Theoretical mechanical properties of strands and cables made of wound carbon nanotube fibers

Theoretical mechanical properties of strands and cables made of wound carbon nanotube fibers

Giovanni MIGLIACCIO

Department of Engineering and Architecture, University of Parma
Parco Area delle Scienze 181/A, I 43100 Parma, Italy

Reginald DES ROCHES

Department of Civil and Environmental Engineering, Rice University
Houston, TX 77005, United States of America

Gianni ROYER-CARFAGNI

Department of Engineering and Architecture, University of Parma
Parco Area delle Scienze 181/A, I 43100 Parma, Italy
and
Construction Technologies Institute - National Research Council of Italy (ITC-CNR)
Viale Lombardia 49, I 20098 San Giuliano Milanese, Italy

Abstract

Thanks to their very high strength-to-weight ratio, Carbon-NanoTube Fibers (CNTFs) hold great promise for challenging structural applications, such as super-long suspension bridges or power lines. Here we present a theoretical model, propaedeutic for an experimental campaign, to describe the mechanical response of stretched and twisted strands/cables made of wound CNTFs. The fibers, to the touch, have a consistency similar to a cotton thread, with dominant axial stiffness over bending stiffness, as

Email addresses: giovanni.migliaccio.it@gmail.com (Giovanni MIGLIACCIO), rdr@rice.edu (Reginald DES ROCHES), Corresponding author: gianni.royer@unipr.it (Gianni ROYER-CARFAGNI)

August 29, 2022

confirmed by microstructurally-motivated models and experiments. Therefore, instead of using the classical Kirchhoff-Love rod model, as usually done for the helical wires in steel cables/strands, the problem is defined in a variational form susceptible to coherent simplifications to obtain closed-form expressions. First, we consider the manufacturing of a strand/cable starting from fibers with a pre-twist, which can be naturally converted in the tortuosity of a helical shape, as done for hemp ropes. From this reference configuration, we define the tensional and torsional response of N-wire strands, with $N = 2, 3, 4, 7$, and of cables made of several concentric layers of helical fibers. In a parametric analysis, the mechanical (stiffness parameters, Poisson's ratio) and geometric (helical pitch) properties of the CNTFs are varied. Expressions are presented for the internal forces associated with the radial interaction among adjacent layers of fibers, which may affect the strength of the fibers and the resilience of the cable. Such forces show a variation with the helical pitch which is opposite to that of the cable axial stiffness, suggesting by insight the existence of an optimal compromise between strength and stiffness, yet to be experimentally verified.

Keywords: Carbon nanotube fibers; helically arranged strand; cable; micromechanical characterization; constitutive properties.

Contents

Nomenclature

CNT	Carbon NanoTube
CNTF	Carbon NanoTube Fiber
ML	Multi-Layer
SS	Self-Similar
$\mathbf{a}_i$	fiber local triad in the reference state, $i = 1, 2, 3$
$\mathbf{b}_i$	fiber local triad in the actual state, $i = 1, 2, 3$
d	nanotube diameter
f_R	radial force on the helical fiber per unit fiber length
$\mathbf{k}$	fiber mechanical curvature vector
$k_{\mathcal{B}_f}$	fiber bending curvature
$k_{\mathcal{T}_f}$	fiber torsion curvature
$k_{\mathcal{B}_f}^{(0)}$	normal curvature of a helical fiber
k_{NT}	shear constant describing interaction among nanotubes
l	nanotube length
p	arc-length of the fiber centre-line in the actual state
$\mathbf{r}_C$	position of the fiber point C lying on the reference centre-line
$\mathbf{r}_{\tilde{C}}$	position of the fiber point $\tilde{C}$ lying on the actual centre-line
$\mathbf{r}_P$	position of the fiber point P in the reference state
$\mathbf{r}_{\tilde{P}}$	position of the fiber point $\tilde{P}$ in the actual state
s	arc-length of the fiber centre-line in the reference state
x, y, z	Cartesian coordinates of fiber axial points
z_α	coordinates of fiber cross-sectional points, $\alpha = 1, 2$
A_f	fiber cross-sectional area
D_f	fiber cross-sectional diameter, $D_f = 2R_f$
F_{R_i}	radial force on a helical fiber of a cable at radial position R_i
L	length of a bundle of CNTFs forming a strand/cable

L_f	fiber length
N	number of fibers of a bundle of CNTFs forming a strand/cable
M	number of layers of fibers in a multi-layer cable
R_f	fiber cross-sectional radius
R_M	cross-sectional radius of a cable made of M layers of fibers
R, φ, u	Cylindrical coordinates of fiber axial points
W	energy density function of CNTF aggregates forming a strand/cable
$W^{(2)}$	part of W containing quadratic terms in ε and β
W_f	energy density function of a single CNTF
β	twist rate of CNTF aggregates forming a strand/cable
η_f	coefficient of decay of strand/cable stiffness with Poisson's ratio ν_f
$\varepsilon_{f\phi}$	strain of fiber ϕ-lines
ε_f	extension of the fiber axis or centre-line
ε	axial extension of CNTF aggregates forming a strand/cable
λ_{NT}	coefficient associated with the CNTF bending stiffness
ϕ	angular coordinate of fiber cross-sectional points
ψ	offset constant describing arrangement of nanotubes in fibers
ν_f	Poisson's ratio describing the fiber cross-sectional contraction
ν_f^*	coefficient of additional contraction of a strand cross-section
σ	tensile strength of a straight fiber
σ_c	tensile strength of a fiber helically wound in a cable
φ, γ, θ	Euler's angles of the triad $\mathbf{b}_i$ with respect to the triad $\mathbf{a}_i$
$\mathcal{B}$	bending stiffness of a bundle of CNTFs forming a strand/cable
$\mathcal{B}_f$	bending stiffness of a single CNTF
$\mathcal{B}_{ref}$	bending stiffness of a reference beam with compact cross-section
$\mathcal{B}_{NT}$	CNT bending stiffness
$\mathcal{E}$	tensile stiffness of a bundle of CNTFs forming a strand/cable

$\mathcal{E}_f$	tensile stiffness of a single CNTF
$\mathcal{E}_{ref}$	tensile stiffness of a reference beam with compact cross-section
$\mathcal{T}$	torsion stiffness of a bundle of CNTFs forming a strand/cable
$\mathcal{T}_f$	torsion stiffness of a single CNTF
$\mathcal{T}_{ref}$	torsion stiffness of a reference beam with compact cross-section

1. Introduction

Since the 1950s, when advanced structures were essentially made of metals [1], there has been an increasing demand, especially in the aerospace sector, for even more performing materials for which key properties are the specific strength and stiffness, i.e., the strength and stiffness per unit specific weight. If in aerospace applications weight saving is a primary concern, for large structures, such as long-span suspension bridges, there is a limit size dictated by material properties, beyond which they shall collapse under their own weight [2, 3]. In fact, as already indicated by Galileo [4, 5], the laws of rescaling for load-bearing structures do not follow the simple geometric proportion, as the structural weight increases more than the structural capacity, and can equally lead to an effective loss of stiffness [6].

Carbon-based materials, such as carbon fiber reinforced polymers, usually perform much better than metals, but the discovery of Carbon NanoTubes (CNTs) in the 1990s [7] has opened up new possibilities, yet to be fully discovered and appreciated. Thanks to their atomic structure, CNTs exhibit a unique combination of physical properties [8–11], including very high specific strength/stiffness and good electrical/thermal conductivity. Therefore, they are perceived as promising basic constituents to produce innovative materials, not only to replace metals in current engineering applications, but also to design structures not even conceivable with what is today available [12, 13]. Applications may include strong yet flexible wearable electronics [14–16], thin and flexible bio-compatible fibers to bridge damaged heart tissues [17], lightweight electrical conductors and shields to replace more heavy copper-based elements [14, 18], structural cables for very long suspension bridges and power lines [6, 12], passing to daring applications in the space industry, such as the Space Elevator[1] project

[1] In 2005, the US National Aeronautics and Space Administration (NASA) launched a "Strong Tether Challenge", aiming to find a tether with a specific strength up to $7.5\,\mathrm{GPa\,cm^3\,g^{-1}}$ for the

[13].

If, on the one hand, CNTs have a high structural capacity, on the other hand their dimensions are very small (diameter and length of the order of 1 nm and $10 - 100$ μm, respectively). Consequently, the problem arises of how to organize CNTs into structural elements for large-scale application. When assembled inside a matrix, their strength becomes impaired by defects, impurities, random orientations, discontinuous lengths, and weakness of the matrix itself. Synthesization through a gas-flow focusing method has permitted to fabricate CNT bundles with tensile strength over 80 GPa [9], but their length remains limited to a few centimetres.

Very promising for large-scale components are the state-of-the-art solution-spun Carbon NanoTube Fibers (CNTF), exhibiting mechanical and electrical properties that compete with both high-strength fibers (such as aramid or carbon fiber) and metallic conductors. Following the breakthrough introduction of aqueous suspension spinning by Poulin's group [20], solution spinning [18] has proved to be effective for the production of CNTFs with highly-aligned densely-packed microstructures of short CNTs (below 10 μm), hereafter termed SS-CNTFs. Current technology [10] allows to manufacture SS-CNTFs with diameter of the order of $100 - 500\,\mu$m and, in principle, no limit in terms of length (several meters for in lab synthesis, but this can be improved in large-scale production). Since there is no matrix that embeds the CNTF constituents (unlike classical carbon fibers), their macroscopic properties could in principle approach those of the CNTs. Indeed, thanks to better production technologies, a constant improvement has already been achieved in the last 20 years. To illustrate, Table 2 reports basic mechanical properties and shows the variation of their value over the years (data taken from Figures 3 and 4 of [10]).

dream of making space elevators [19]. There is no winner for this challenge yet.

Fiber Year	σ [GPa]	E [GPa]	γ [kN/m3]	σ/γ [km]	E/γ [Mm]
SS-CNTF 2004	0.1	110	11.2	8.9	9.8
SS-CNTF 2013	1.0	110	17.0	58.9	6.5
SS-CNTF 2020	4.2	260	19.6	214.3	15.1

Table 2: Mechanical properties of Solution-Spun Carbon-Nanotube Fibers (SS-CNTFs): tensile strength σ [GPa], Young's modulus E [GPa], specific weight γ [kN/m3] (values obtained from Figures 3 and 4 of [10]). Indexes of structural performance are represented by the specific strength σ/γ and specific stiffness E/γ, for which one can observe a constant improvement over the years.

To the touch, SS-CNTFs are similar to a cotton thread: they are lightweight, highly flexile, more conductive than stainless steel and much stronger than copper. Experiments [21] have evidenced that their high axial stiffness is dominant over the bending stiffness. This is consequent to the particular microstructural organization of the fibers, which consists of aligned CNTs, bonded one another along their lateral surface by Van der Waals forces. It has been theoretically demonstrated [22] that the tensile and flexural capacities of the fibers are dictated, more than by the properties of the CNTs, by the compliance of the lateral bond and, in particular, by the offset between adjacent CNTs, which affects the resultant of the lateral contact forces. Therefore, it is expected that improvements in the production techniques will allow denser packaging of longer CNTs with optimal offset, increasing the strength of the lateral bond to achieve mechanical properties close to those of CNT bundles.

The availability of long CNTFs with exceptional properties can allow to manufacture structural elements with capacities far superior to their metallic competitors. To this respect, the most important property is represented by the specific strength, or breaking length, defined as the ratio between the material strength σ and specific weight γ. As discussed at length in [6], this parameter determines how much the capacity of the material is dissipated in bearing the structural self-weight in addition to the service load in a large structure. Another important index [6] is represented by

the specific stiffness, i.e., the ratio between Young's modulus E and γ. This dictates the effects of the self-weight on structural stiffness, as in the paradigmatic example of the inclined cables of a cable stayed bridge, for which the effective stiffness is interpreted via Ernst's formula [23]. Values of σ/γ and E/γ are reported in Table 2 for various types of CNT fibers.

Just as high-strength steel wires are arranged in strands and multi-layer cables to obtain long structural elements, CNTFs shall also be organized in a similar way. However, there are substantial differences. The bending stiffness of CNTFs is typically very low, much lower than the expected value predicted by Euler-Bernoulli beam theory. Careful experiments [21] have shown that, whereas steel wires show a bending stiffness that scales proportionally to the tensile Young's modulus and to the fourth power of the diameter, the bending stiffness of CNTFs exhibits a power law dependence on the fiber diameter with exponent comprised between two and four. As it will be discussed in Section 2.1, this is due to the compliance of the lateral bond, which produces the shearing of the CNTs [22]. The consequence, at the macroscopic level, is that the bending response results intermediate between the limit cases of perfect sliding (power law the cross sectional radius with exponent two) and perfect coupling (exponent four).

Strands/cables made of metallic wires are usually studied by means of models in which the force and moment resultants on the end sections are obtained by summing up the relevant actions on the constituent wires [24–26]. The wires are in general considered to be curved rods in the natural state [27–30], whose mechanical behavior is governed by force and moment balance equations [31–34], according to the Kirchhoff-Love rod theory [35]. A wide list of references about the modelling of metallic strands/cables can be found in review articles [36–39], which also recall expressions in closed-form for the stiffness of strands/cables under uniaxial loads. Among them, we recall theories

within three categories: models based on purely tensile wires, such as that proposed by Hruska [37, 40]; models which incorporate the effect of the wire bending/torsional stiffness, such as the simple model by Mc-Connel and Zemke [38], as well as those by Sathikh et al. [41] and Labrosse et al. [42]; models that also account for the cross-sectional contraction of the metallic wires (Poisson effect), such as those by Kumar and Cochram [43], and by Foti and Martinelli [44].

A theoretical model, propaedeutic to design a targeted experimental campaign, is here presented to define the mechanical properties of strands and cables made of wound CNTFs. The characterization of the mechanical properties of CNTFs based on the description, at the micro-scale, of the arrangement of the constituent CNTs has been considered in previous work [21, 22]. Here, our analysis is at the mesoscopic lengh-scale: given the extensional, bending and torsional properties of the single fiber, we consider the organization of multiple fibers in the form of straight strands and cables, and we derive the corresponding mechanical properties under uniaxial load. Since the fibers are wound on each other in helical shapes, we derive a coupled dependence between extensional and torsional stiffness. The strands/cables made of such fibers present a consistency similar to what they would have if they were made from vegetable fibers. The manufacturing technique is similar to that for a hemp rope: first, individual CNTFs are pulled and pre-twisted; then, they are brought closer and wound together in such a way that the pre-twist of a straight fiber turns into the tortuosity of a helical line [14]. In general, the mechanical behavior of these strands/cables is dominated by the axial stiffness of the constituent fibers. The bending stiffness is too small to have a significant role [22], but the torsional properties come into play, at least in the manufacturing phase.

The proposed modelling approach starts from the manufacturing step, to determine the reference configuration for the fibers forming the strand/cable. After demonstrat-

ing that the reference shape is a helix (this is not assumed a priori, as in classical works on metallic wires, but derived from variational principles), we discuss the equivalence between the fiber cross-sectional twist and the tortuosity-induced twist, which is useful for manufacturing. Then, we calculate the tensile and torsional stiffness of the assembly as a function of the mechanical properties of the constituent CNTFs and of their geometry (helical pitch) in the reference state. Instead of using classical approaches based on force and moment equilibrium equations, the problem is defined in a variational form, which provides a unified formulation susceptible of coherent simplifications to obtain approximate expressions in closed form for stiffness and strength parameters. Within the proposed approach, the CNTF deformation is described by macroscopic indicators of strain, which are proved to be associated, in a mechanical analogy, with the extension and curvatures of an equivalent rod. Using geometric symmetry, it is possible to recognize the equilibrium states of the single fiber, without a direct definition of the contact forces associated with the interaction between adjacent fibers. These forces, however, can be recovered a posteriori and are of importance because they can affect the strength of the fibers and the resilience of the cable. Such forces show a variation with the helical pitch which is opposite to that of the cable axial stiffness, suggesting by insight the existence of an optimal strength/stiffness compromise, yet to be experimentally verified.

In section 2, we define the equivalent rod model for the single CNTF based on macroscopic descriptors of strain (extension, curvature, twist), motivated by the recalled micromechanics of the constituent CNTs. The equilibrium states are defined for a paradigmatic model problem, motivated by geometric symmetry. In section 3, we discuss the manufacturing process for N-wire strands, with $N = 2, 3, 4, 7$, and for cables made of concentric layers of wound fibers. Hence, we theoretically derive extensional and torsional properties of the strand/cable as a function of the geometric arrangement of the CNTFs. In the parametric analysis of section 4, the mechanical

(axial/bending/torsional stiffness, Poisson's ratio) and geometric (helical pitch) properties of the CNTFs are made to vary. The weak dependence on some parameters suggests simplifications in the theory, such as to obtain closed-form expressions for dimensionless parameters describing the axial stiffness of the strand/cable and the stress state in the constituent CNTFs. The main results of this study, together with possible future developments, in particular as regards the design of an experimental campaign on full-scale prototypes, are summarized in the Conclusions Section.

2. Mechanical modelling of CNT fibers

Before analyzing the response of a group of wound CNTFs, it is necessary to consider first a single fiber. This is modeled as an equivalent rod, for which the extensional, flexural and torsional stiffnesses can be derived from the micromechanics of the constituent CNTs, as is discussed in [22]. The case of one CNTF wrapped around a cylindrical mold, solved for appropriate boundary conditions, is then introduced as the model problem for analyzing arrangements of multiple CNTFs.

2.1. Micromechanics of CNT fibers

Consider a CNTF of length L_f and cross section A_f, composed by a mono-dispersed assembly of CNTs of length $l \ll L_f$ and diameter $d \ll D_f$. Figure 1 schematically shows the CNTs composing the fiber in a regular arrangement.

Experiments [10, 21] have provided evidence that the axial stiffness of a fiber of this kind is much lower than the sum of those of the CNTs that make up the cross section. This suggests that the CNTs are not perfectly linked to each other: the macroscopic elongation of the fiber is due not only to the straining of the CNTs, but also to their relative slipping along the lateral surface [22, 45, 46].

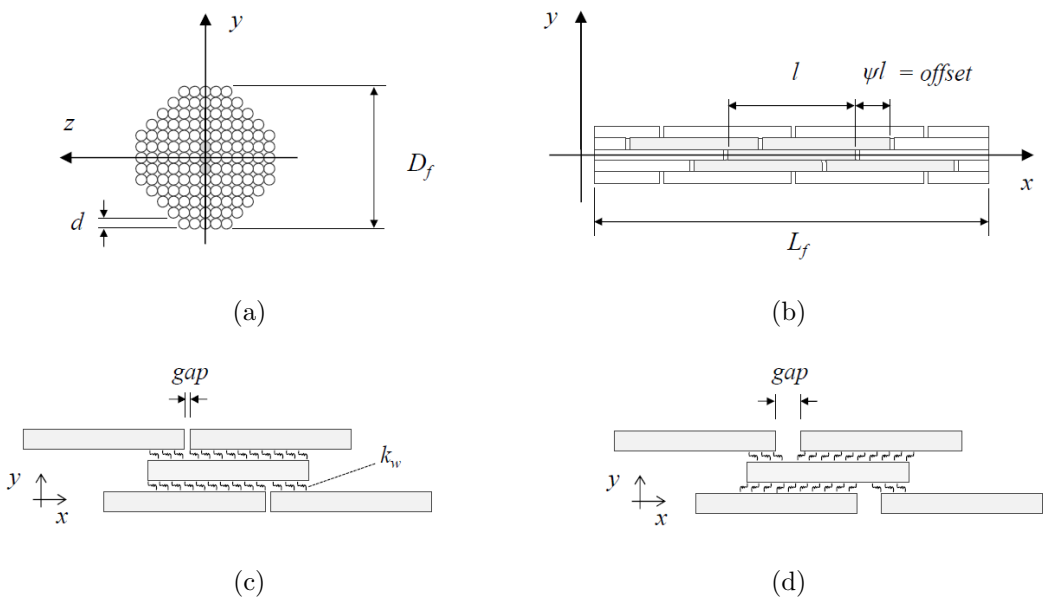

Figure 1: Fiber composed by mono-dispersed CNTs: (a) cross-section with the CNTs arranged in a square lattice; (b) longitudinal arrangement of the CNTs, with indication of their offset ψl. Spring-based model to describe the lateral interaction between CNTs: (c) undistorted state and (d) strained state of the fiber, with longitudinal rearrangement of the CNTs due to the relative slipping.

Various models [45, 47, 48] have been proposed to predict the mechanical properties of CNTFs. In [22], the CNTs are supposed to be aligned along lines parallel to the fiber axis, with constant offset ψl between any pair of CNTs and in such a way that, at each cross-section, their centers form a regular square lattice, as indicated in Figure 1(a-b). The CNTs interact only along their lateral surface, by means of distributed shear forces proportional to their relative slipping, as for a layer of shear springs with stiffness constant k_{NT}. The mechanical properties of the CNTF, in particular the tensile stiffness $\mathcal{E}_f$, are dictated by the longitudinal re-arrangement of the CNTs when the fiber is pulled, as schematically shown in Figure 1(c-d). If the strain in the CNTs is neglected, which is a reasonable hypothesis since the shear coupling is much more compliant than the CNT axial stiffness, one can demonstrate [22] that

$$\mathcal{E}_f = 2k_{NT}\psi(1-\psi)(l/d)^2 A_f\,. \tag{2.1}$$

Therefore, the tensile stiffness $\mathcal{E}_f$ depends on the aspect ratio l/d of the CNTs, the offset parameter $\psi \in (0,1)$, and the stiffness of the interface k_{NT} .

Similarly , shear coupling and re-arrangement of the CNTs when the fiber is bent, as per Figure 2, provide the fiber bending stiffness $\mathcal{B}_f$. If the fiber cross section is approximately a circle of radius R_f, $\mathcal{B}_f$ can be expressed [22] in the form

$$\mathcal{B}_f = (k_{NT}\lambda_{NT} + \mathcal{B}_{NT}/d^2)A_f\,, \tag{2.2}$$

where $\mathcal{B}_{NT}$ is the bending stiffness of a CNT, modelled as an Euler-Bernulli beam, whereas λ_{NT} is a coefficient that depends on the lengths and diameters of fiber and CNTs. The fiber bending stiffness is intermediate between two limit conditions: i) when $L_f/R_f \ll l/d$, then $\lambda_{NT} \to L_f^2/12$; ii) for $L_f/R_f \gg l/d$, one finds that $\lambda_{NT} \to \psi(1-\psi)(l/d)^2 R_f^2/2$. In the first condition, the CNTs can freely slide one another, as if $k_{NT} \simeq 0$, and $\mathcal{B}_f$ is proportional to R_f^2 (*layered limit*). The second case corresponds to a rigid coupling between the CNTs: the fiber behaves like a beam of compact cross section, such that $\mathcal{B}_f$ is proportional to R_f^4 (*monolithic limit*).

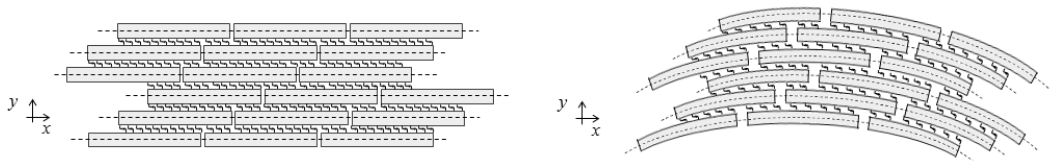

(a) (b)

Figure 2: Fiber composed by mono-dispersed CNTs: (a) undistorted state for the longitudinal arrangements of the CNTs; (b) rearrangement under bending.

There is a good agreement between theory and experiments [21, 22]. In general, the bending stiffness $\mathcal{B}_f$ approaches the layered limit and is very low with respect to the axial stiffness $\mathcal{E}_f$. Typical values of the axial stiffness $\mathcal{E}_f$ of fibers of this kind, with diameter $D_f = 22\,\mu$m, are in the range $27.5 - 52.4\,$N mm/mm, when the length of the constituent CNTs are of the order of $l = 2.21 - 6.28\,\mu$m and the CNT diameter is $d = 1.5\,$nm. For the bending stiffness $\mathcal{B}_f$, instead, one finds that the dimensionless parameter $\mathcal{B}_f/(\mathcal{E}_f D_f^2)$ is in the interval $(0.01, 0.05)$, justifying the dominant influence of the axial stiffness $\mathcal{E}_f$ on the mechanical behavior of such fibers.

A third important deformation state is that in which the fiber end sections are relatively rotated apart of the twist angle βL_f, where β is the twist rate. The torsional stiffness $\mathcal{T}_f$ should again be dictated by the shear coupling of the fiber CNTs. It is expected that $\mathcal{T}_f$ is intermediate between the limit cases of decoupled behavior (*layered limit*), in which it is the simple sum of the torsional stiffnesses of the CNTs, and rigid shear coupling (*monolithic limit*), in which the cross section compactly rotates. To the best of our knowledge, very little attention has been paid to the experimental measurement of the torsional stiffness of CNTFs and to the complementary mechanical modelling. Most probably, this is because, in most applications, this property does not come into play, but we will show that it becomes important when considering the response of strands and cables made of CNTFs. While postponing to a forthcoming work the experimental activity and the modelling, our purpose, here, is to investigate, in a parametric analysis, how the tensile capacity of strands and cables made of wound CNTFs is affected by the mesoscopic properties of the fibers, represented by the tensile stiffness $\mathcal{E}_f$, the bending stiffness $\mathcal{B}_f$ and the torsional stiffnesses $\mathcal{T}_f$.

2.2. Deformation at the fiber level

Consider fibers having the shape of a rod, generated by moving a circle of radius R_f (fiber cross-section) along a line (fiber axis or centerline) of length L_f, as in

Figure 3. The fiber diameter $D_f = 2R_f$ is much smaller than the axial length L_f. The cross-sections are orthogonal to the fiber axis in the natural undistorted state, supposed straight, and remain plane and orthogonal to the centerline in the deformed configuration. In the following, summation convention is used: the Latin indices take the values 1, 2, 3, while the Greek indices the values 1, 2.

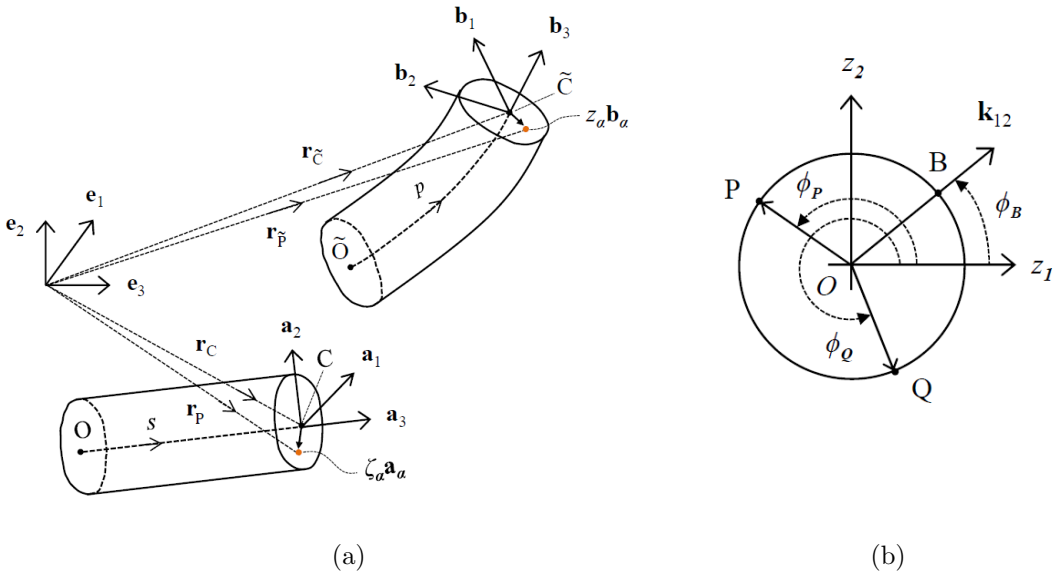

(a) (b)

Figure 3: (a) Schematics of a fiber element in the natural undistorted reference state and in the deformed actual state. (b) Cross-sectional plane with local coordinates z_1-z_2, with indication of the projection $\mathbf{k}_{12}$ of the mechanical curvature vector $\mathbf{k}$.

Figure 3 shows a fiber element in the natural undistorted *reference* state (a) and in its deformed *actual* state (b). With respect to an orthogonal reference frame $(\mathbf{e}_1, \mathbf{e}_2, \mathbf{e}_3)$, the position of the generic point P of the fiber in the reference state and of its image $\widetilde{P}$ in the actual state are respectively defined by the vectors $\mathbf{r}_P$ and $\mathbf{r}_{\widetilde{P}}$. Similarly, the positions of the points C and $\widetilde{C}$ lying on the reference and actual centerlines are identified by $\mathbf{r}_C$ and $\mathbf{r}_{\widetilde{C}}$, as well as by the curvilinear coordinates (arc-length) s and p.

Observe that s coincides with p only if the centreline is inextensible; more in general, $p = p(s)$ is a function of s. It is useful to introduce the *local* triad $\mathbf{a}_i$, $i = 1, 2, 3$, in the reference state, with $\mathbf{a}_3$ overlapping with the straight centerline, as well as its image $\mathbf{b}_i$ in the actual state, with $\mathbf{b}_3$ tangent to the deformed centerline.

Suppose that the *cross sections remain undistorted* during the deformation. Then, let z_α, $\alpha = 1, 2$ represent local coordinates in the cross sectional plane, in such a way that the positions of the points P and $\widetilde{P}$ with respect to C and $\widetilde{C}$ are defined by

$$\mathbf{r}_P = \mathbf{r}_C + z_\alpha \mathbf{a}_\alpha \,, \quad \mathbf{r}_{\widetilde{P}} = \mathbf{r}_{\widetilde{C}} + z_\alpha \mathbf{b}_\alpha \,. \tag{2.3}$$

The constitute response of the fiber is characterized via three independent indicators of strain, namely the axial extension ε_f, the bending curvature $k_{\mathcal{B}_f}$, and the torsion curvature $k_{\mathcal{T}_f}$. The analytical description of these quantities is based on the results of a "thought experiment", in which we imagine to measure the local elongation along curves lying on the lateral surface of the fiber when this is deformed. This could be done, e.g., by means of micro strain gages, ideally placed at specific points of the curve in the direction of the tangent line.

To explicit the calculation, consider a surface curve in the reference state corresponding, at each section $s \in (0, L_f)$, to points identified by the coordinates

$$z_1 = R_f \cos\left(\phi(s)\right) , \; z_2 = R_f \sin\left(\phi(s)\right) , \; s \in (0, L_f) \,, \tag{2.4}$$

where $\phi(s)$ is a function that will be defined later on, according to the specific cases. This relationship defines the functions $\mathbf{r}_{P\phi}(s)$ and $\mathbf{r}_{\widetilde{P}\phi}(s)$, which indicate the position of the points P and $\widetilde{P}$ laying on such a line at the cross section s, respectively in the reference and actual state.

The local strain $\varepsilon_{f\phi}(s)$ measured at s, in the tangent direction to the curve, reads

$$\varepsilon_{f\phi}(s) = \frac{\|d\mathbf{r}_{\widetilde{P}\phi}(s)\|}{\|d\mathbf{r}_{P\phi}(s)\|} - 1 = \frac{\|\mathbf{r}'_{\widetilde{P}\phi}(s)\|}{\|\mathbf{r}'_{P\phi}(s)\|} - 1 \tag{2.5}$$

where $\|\cdot\|$ is the Euclidean norm and prime ($'$) denotes s-derivative. In particular, from (2.3) and (2.4), one finds

$$\mathbf{r}'_{P\phi} = \mathbf{a}_3 + R_f\phi' \left(-\sin\phi\,\mathbf{a}_1 + \cos\phi\,\mathbf{a}_2\right), \tag{2.6a}$$

$$\mathbf{r}'_{\widetilde{P}\phi} = p'\mathbf{b}_3 + R_f\phi' \left(-\sin\phi\,\mathbf{b}_1 + \cos\phi\,\mathbf{b}_2\right) + R_f\mathbf{k} \times \left(\cos\phi\,\mathbf{b}_1 + \sin\phi\,\mathbf{b}_2\right), \tag{2.6b}$$

where $\times$ is the usual vector product, $p' = dp/ds$ is the centre-line stretch, and $\mathbf{k}$, referred to as *mechanical curvature vector*, is a function of s and is defined by

$$\mathbf{b}'_i(s) = \frac{d\mathbf{b}_i}{ds}(s) = \mathbf{k}(s) \times \mathbf{b}_i(s)\,. \tag{2.7}$$

In general, when the rod is bent and stretched, the mechanical curvature $\mathbf{k}$ multiplied by the stretch p' provides the usual geometric curvature, $\mathbf{k}_g = p'\,\mathbf{k}$. The mechanical curvature $\mathbf{k}$ allows one to isolate curvature variations associated with bending from curvature variations produced by stretching, as remarked by [49]. The mechanical meaning of $\mathbf{k}$ is also discussed in [50, 51] for beams under plane deformation and in terms of work conjugation and principle of virtual work. Hereafter, a direct interpretation for spatial beams is provided by discussing its relation with the indicators of strain, $\varepsilon_f(s)$, $k_{\mathcal{B}_f}(s)$, $k_{\mathcal{T}_f}(s)$, mentioned in the foregoing. In particular, according to a classical experimental practice [52], the *bending curvature* $k_{\mathcal{B}_f}(s)$ at the cross section s is related to the difference between the local strains measured on two diametrically opposite lines, parallel to the fiber axis in the reference state, divided by the diameter of the fiber: the plane of principal bending is identified by those lines that provide

the maximum absolute value of such difference. Similarly, the *extension* $\varepsilon_f(s)$ at s is associated with half the sum of the aforementioned strain measures, which is the same whatever the two diametrically-opposite lines considered. Finally, the *torsion curvature* $k_{\mathcal{T}_f}(s)$ at s is calculated by considering the difference between the surface local strains along two orthogonal directions, initially at 45° with respect to the fiber axis, and dividing the result by the fiber radius: the result shall be independent of the point of the cross sectional border where the measurement is taken.

Consider two lines defined via (2.4) by setting either $\phi(s) = \phi_0$ or $\phi(s) = \phi_0 + \pi$. Therefore, $k_{\mathcal{B}_f}(s)$ shall be defined as

$$k_{\mathcal{B}_f}(s) = \max_{\phi_0} \left(\lim_{R_f \to 0} \frac{\varepsilon_{f\phi_0}(s) - \varepsilon_{f\phi_0+\pi}(s)}{2R_f} \right) . \tag{2.8}$$

By using the definition (2.8) and equations (2.4)-(2.6), the final result is that

$$k_{\mathcal{B}_f}(s) = \mathbf{k}(s) \cdot \mathbf{b}_B(s), \text{ for } \phi_0 = \phi_B(s) + \pi/2 \, . \tag{2.9}$$

Here, the angle $\phi_B(s)$ identifies the direction of the projection of $\mathbf{k}(s)$ on the cross-sectional plane z_1-z_2 at s, as indicated in Figure 3(c), whereas $\mathbf{b}_B(s) = \cos\phi_B \, \mathbf{b}_1(s) + \sin\phi_B \, \mathbf{b}_2(s)$. The angle $\phi_B(s)$ identifies the plane of bending at each section s.

The extension $\varepsilon_f(s)$ is given by

$$\varepsilon_f(s) = \lim_{R_f \to 0} \frac{\varepsilon_{f\phi_0} + \varepsilon_{f\phi_0+\pi}}{2} = p' - 1, \ \forall \, \phi_0 \, , \tag{2.10}$$

and it is found to be independent of the choice of ϕ_0.

To calculate $k_{\mathcal{T}_f}(s_0)$ at the cross section $s = s_0$, consider the point that corresponds to the intersection of two helical curves, defined in (2.4) by $\phi(s) = \phi_1(s) = \phi_0 + (s -$

$s_0)/R_f$ and $\phi(s) = \phi_2(s) = \phi_0 - (s - s_0)/R_f$, where ϕ_0 is arbitrary. One has

$$k_{\mathcal{T}_f}(s_0) = \lim_{R_f \to 0} \frac{\varepsilon_{f\phi_1}(s_0) - \varepsilon_{f\phi_2}(s_0)}{R_f} \,. \tag{2.11}$$

Again, by using definition (2.11) and equations (2.4)-(2.6), it is possible to show that the result is independent of the choice of ϕ_0 and reads

$$k_{\mathcal{T}_f}(s_0) = \left(\frac{2}{1 + (p'(s_0))^2} \right)^{1/2} \mathbf{k}(s_0) \cdot \mathbf{b}_3(s_0), \quad \forall\, \phi_0 \,. \tag{2.12}$$

This demonstrate that that $k_{\mathcal{T}_f}$ is proportional to the component of $\mathbf{k}$ on the tangent to the deformed centerline, and coincides with it when the axial extension is negligible, i.e., when $p' \simeq 1$.

In the previous derivations, the cross sections of the rod have been supposed to remain undistorted; the formulas become more complicated if one considers the cross sectional contraction, variable at each point of the cross section. A more general rod model could account for the in-plane and out-of-plane cross-sectional deformation, as discussed in [53, 54]. For the purpose of the present work, an approximate "average" estimate of the cross-sectional deformation is considered sufficient. This can be obtained by considering only the effects of the centre-line extension $\varepsilon_f(s)$, so that a circular cross section remains circular but with a different radius. Assuming that the fiber is linear elastic and denoting with ν_f the Poisson's ratio associated with the cross-sectional contraction, the expression of $\mathbf{r}_{\tilde{P}}$ appearing in (2.3) should be substituted by

$$\mathbf{r}_{\tilde{P}} = \mathbf{r}_{\tilde{C}} + (1 - \nu_f \varepsilon_f) z_\alpha \mathbf{b}_\alpha \,, \tag{2.13}$$

The same factor $(1 - \nu_f \varepsilon_f)$ would consequently appear in the expressions (2.9) and (2.12), respectively for $k_{\mathcal{B}_f}$ and $k_{\mathcal{T}_f}$.

In the particular case in which the fiber extension ε_f is small, so that $p' \simeq 1$ and $1 - \nu_f \varepsilon_f \simeq 1$, the components of $\mathbf{k}$ in and out of the fiber cross-sectional plane coincide with $k_{\mathcal{B}_f}$ and $k_{\mathcal{T}_f}$, respectively. In this case, alternative expressions can be provided for $k_{\mathcal{B}_f}$ and $k_{\mathcal{T}_f}$, which will be useful for the following developments. To this aim, we exploit the fact that $\mathbf{k}$ is related to the change of orientation of $\mathbf{b}_i$ along the fiber axis: $k_{\mathcal{T}_f}$ coincides with the component of $\mathbf{k}$ along $\mathbf{b}_3$, while $k_{\mathcal{B}_f}$ is the projection of $\mathbf{k}$ on the cross section (orthogonal to $\mathbf{b}_3$).

Specifically, we introduce three Euler's angles, φ, γ, θ, that define the relative orientation between $\mathbf{b}_i$ and $\mathbf{a}_i$ (see, e.g., [55–57]). These angles represent rotations to bring the triad $\mathbf{a}_i$ to coincide with $\mathbf{b}_i$: first rotation of intensity φ about $\mathbf{a}_2$, second rotation equal to γ about $\mathbf{a}_R = -\cos\varphi\,\mathbf{a}_1 + \sin\varphi\,\mathbf{a}_3$, and third rotation of magnitude θ about $\mathbf{b}_3$. In general, φ, γ, θ depend on s and the following relation holds

$$\mathbf{k} = \varphi' \mathbf{a}_2 + \gamma' \mathbf{a}_R + \theta' \mathbf{b}_3 \,. \tag{2.14}$$

We can thus write $k_{\mathcal{B}_f}$ and $k_{\mathcal{T}_f}$ in the form

$$k_{\mathcal{B}_f} = \sqrt{(\mathbf{k} \cdot \mathbf{b}_1)^2 + (\mathbf{k} \cdot \mathbf{b}_2)^2} = \sqrt{(\gamma')^2 + (\varphi' \cos\gamma)^2} \,, \tag{2.15}$$

$$k_{\mathcal{T}_f} = \mathbf{k} \cdot \mathbf{b}_3 = \theta' + \varphi' \sin\gamma \,. \tag{2.16}$$

These expressions describe the macroscopic deformation of the fiber and will be used in the following sections.

2.3. Equilibrium at the fiber level

Consider fibers organized in hierarchical structures to form strands and cables: typical arrangements are represented in Figure 4(a), which shows Multi-Layer (ML) cables made of 1, 2, and 3 layers of helically wound fibers. Our aim is to model the mechanical behavior under uniaxial loads of cables of this kind made of carbon-nanotube fibers. Observe that in the case of SS-CNTFs, the fiber axial stiffness $\mathcal{E}_f$ plays a dominant role, since the bending stiffness $\mathcal{B}_f$ is generally small [21, 22], and we expect that this is the case also for the torsional stiffness $\mathcal{T}_f$. However, in a more general model, we do not neglect the contribution of $\mathcal{B}_f$ and $\mathcal{T}_f$, whose importance will be discussed a posteriori. The torsional stiffness, in particular, will play an important role in the manufacturing of strands/cables made of helically wound fibers.

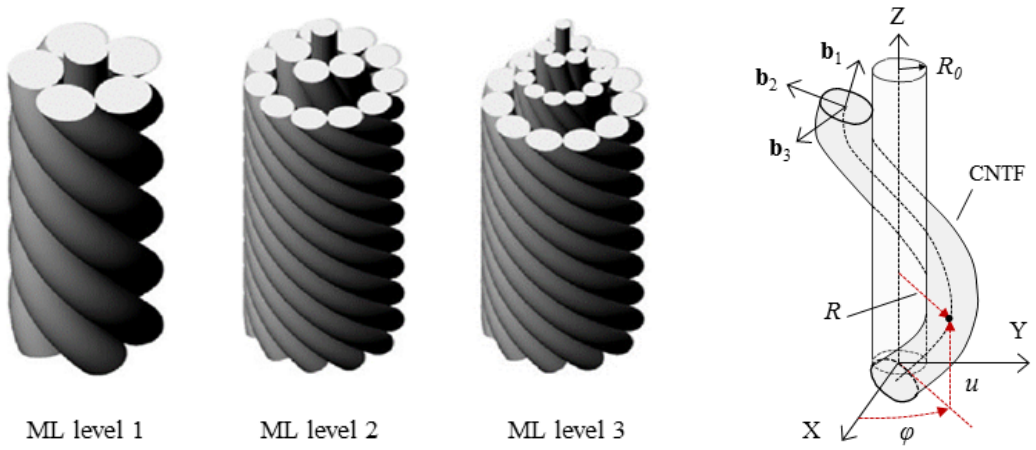

(a) (b)

Figure 4: (a) Hierarchical arrangements of fibers helically wound in a cable: basic arrangement or arrangement of level 1, with fibers wound around a straight central fiber (ML level 1), and arrangements of levels 2 and 3, with two and three layers of wound fibers (ML level 2 and 3). (b) Basic problem of a fiber with circular cross section of diameter $D_f = 2R_f$ and length L_f, wound around a straight cylinder of radius R_0 ($R = R_0 + R_f$).

The basic problem, represented in Figure 4(b), consists in studying the equilibrium configurations of a fiber of length L_f, diameter D_f, and stiffness parameters $\mathcal{E}_f$, $\mathcal{B}_f$, and $\mathcal{T}_f$, initially straight in the undistorted configuration, when it is stretched and wound around a cylinder of radius R_0.

If the cable is evenly and uniformly stretched, the deformation of all the fibers respects the symmetry of the problem: since the wound fibers belonging to the same layer all deform together, the frictional forces between them can be considered small. Therefore, we assume that the CNTF represented in Figure 4(b) is in frictionless contact along its entire length with the cylinder: this hypothesis will be verified later on when we will demonstrate that, for particular geometric arrangements, all the fibers, independently of the layer they belong to, are equally strained. The problem consists in finding the equilibrium state of the fiber when its ends are displaced in given positions, under the constraint that the distance R of the points of the fiber centerline from the cylinder axis does not vary along the length of the cylinder.

The problem is treated with a variational approach. From Section 2.2, the energy density function W_f can be expressed in terms of $\mathcal{E}_f$, $\mathcal{B}_f$ and $\mathcal{T}_f$, in the form

$$W_f = \frac{1}{2}\mathcal{E}_f\varepsilon_f^2 + \frac{1}{2}\mathcal{B}_f k_{\mathcal{B}_f}^2 + \frac{1}{2}\mathcal{T}_f k_{\mathcal{T}_f}^2 \,. \tag{2.17}$$

With respect to the reference frame (X, Y, Z) indicated in Figure 4(b), the actual configuration of the point s on the centerline of the fiber is expressed by

$$x = R\cos\varphi(s), y = R\sin\varphi(s), z = u(s)\,, \tag{2.18}$$

with $s \in (0, L_f)$, where $\varphi(s)$ is the angular coordinate.

It can be directly demonstrated that ε_f reads

$$\varepsilon_f = \sqrt{(R\varphi')^2 + (u')^2} - 1\,. \tag{2.19}$$

Moreover, if one neglects the axial straining of the fiber centerline in the expressions of $k_{\mathcal{B}_f}$ and $k_{\mathcal{T}_f}$, as discussed in Section 2.2, from (2.15)-(2.16) one can write

$$k_{\mathcal{B}_f} = R\frac{\sqrt{(u''\varphi' - u'\varphi'')^2 + (\varphi')^4((R\varphi')^2 + (u')^2)}}{(R\varphi')^2 + (u')^2}\,, \tag{2.20a}$$

$$k_{\mathcal{T}_f} = \theta' + \frac{u'\varphi'}{\sqrt{(R\varphi')^2 + (u')^2}}\,. \tag{2.20b}$$

where we recall that θ' represents the rate of rotation of the local triad $\mathbf{b}_i$ about the direction $\mathbf{b}_3$ tangent to the actual centre-line of the fiber, and $u' = R\varphi'\tan\gamma$.

When the functions $\varphi(s)$, $u(s)$, $\theta(s)$ are prescribed at $s = 0$ and at $s = L_f$ (geometric boundary conditions), the variational problem reduces to

$$\int_{L_f} \delta W_f \, ds = 0\,. \tag{2.21}$$

Denoting, as before, s-differentiation with $'$, the first variation of the functional provides the system of differential equations [58] in the standard form

$$\frac{\partial W_f}{\partial \varphi} - \left(\frac{\partial W_f}{\partial \varphi'}\right)' + \left(\frac{\partial W_f}{\partial \varphi''}\right)'' = 0\,,\ s \in (0, L_f)\,, \tag{2.22a}$$

$$\frac{\partial W_f}{\partial u} - \left(\frac{\partial W_f}{\partial u'}\right)' + \left(\frac{\partial W_f}{\partial u''}\right)'' = 0\,,\ s \in (0, L_f)\,, \tag{2.22b}$$

$$\frac{\partial W_f}{\partial \theta} - \left(\frac{\partial W_f}{\partial \theta'}\right)' = 0\,,\ s \in (0, L_f)\,, \tag{2.22c}$$

with natural boundary conditions

$$\frac{\partial W_f}{\partial \varphi''} = 0\,,\ s = 0, L_f\,, \tag{2.23a}$$

$$\frac{\partial W_f}{\partial u''} = 0\,,\ s = 0, L_f\,. \tag{2.23b}$$

It is possible to directly verify that the problem admits the particular solution

$$\varphi'(s) = \text{const},\ u'(s) = \text{const},\ \theta'(s) = \text{const}\,,\ \ s \in (0, L_f)\,. \tag{2.24}$$

This means that, in the equilibrium state, the central line of the fiber is a helix with a constant pitch, whose cross-sections undergo a constant twist. Hence, $k_{\mathcal{B}_f}$ and $k_{\mathcal{T}_f}$ can be rewritten in terms of the constant slope angle γ of the helix, in the form

$$k_{\mathcal{B}_f} = \varphi' \cos\gamma\,, \tag{2.25a}$$

$$k_{\mathcal{T}_f} = \theta' + \varphi' \sin\gamma\,, \tag{2.25b}$$

where $\tan\gamma = u'/(R\varphi') = \text{const}$.

It is important to observe from (2.25b) that the torsion curvature $k_{\mathcal{T}_f}$ is composed of two contributions: *i*) the "cross-sectional twist" associated with the relative rotation of the cross sections, as per θ', and *ii*) the "tortuosity-induced twist" of the fiber centerline, described by $\varphi' \sin\gamma$. The fiber is torsion free when

$$\theta' = -\varphi' \sin\gamma\,. \tag{2.26}$$

This condition will play an important role when we will discuss (in Section 3.1.1) the manufacturing of strands and cables made of helically-wound fibers, which consists in inducing a "sectional pre-twist" in straight fibers, which is successively transformed in "tortuosity" for their helical configuration within the cable.

In section 2.1 it was shown that the mechanical properties of the fiber are due to the longitudinal bond of the constituent CNTs, which is certainly influenced by transversal forces, orthogonal to the fiber axis, compacting the CNTs together. Furthermore, the transverse contact forces can affect the ultimate capacity of a group of fibers wound together because, in the event of a fiber break, the relevant frictional forces with the other fibers can allow to recover the contribution of the broken filament, at a certain distance from the critical section. Therefore, it is of interest to calculate the transverse forces per unit fiber length $f_R = f_R(s)$, representing the reactions exerted by the cylinder on the fiber wound around it, in the direction orthogonal to the axis of the cylinder of Figure 4(b). The value of f_R is determined by performing a perturbation δR of the radius R of the cylinder around the solution defined by (2.18) and (2.24). This will affect the value of the strain energy density (2.17) because the expressions for the fiber extension and curvatures, given by (2.19) and (2.20), will now carry the dependence upon $R = R(s)$ and its derivatives. The weak form of the equilibrium equations reads

$$\int_{L_f} \delta W_f \, ds - \int_{L_f} f_R \, \delta R \, ds = 0 \,. \tag{2.27}$$

In other words, f_R is obtained by considering the first variation of W_f with respect to a variation $\delta R(s)$ of $R(s)$ around $R(s) = R$.

The expression for f_R can be obtained by solving the problem corresponding to the variational condition (2.27). However, for the purpose of the present work, a reason-

able approximation can be obtained by considering in the expression (2.17) of W_f only the part of the energy that depends on the axial stiffness $\mathcal{E}_f$. This simplification is justified by the fact that, in a very taut fiber, the axial contribution is dominant, also taking into account that the bending stiffness $\mathcal{B}_f$ and the torsional stiffness $\mathcal{T}_f$ are very small, as discussed in Section 2.1.

Considering only the extensional contribution proportional to $\mathcal{E}_f$, the strain energy density W_f takes the form

$$W_f = \frac{1}{2}\mathcal{E}_f\varepsilon_f^2 = \frac{1}{2}\mathcal{E}_f\big(\sqrt{(R')^2 + (R\varphi')^2 + (u')^2} - 1\big)^2\,, \tag{2.28}$$

and from (2.27) one obtains

$$f_R = \mathcal{E}_f\varepsilon_f\frac{\cos^2\gamma}{R}\,. \tag{2.29}$$

where $\mathcal{E}_f\varepsilon_f$ represents the tensile force in the fiber, while $\cos^2\gamma/\,R$ denotes the fiber normal curvature, which coincides with the component of the curvature vector in the radial direction, orthogonal to the axis of the helix.

3. Organized hierarchical arrangements of fibers

Figure 4(a) shows examples of helically arranged fibers. The simplest one is the Multi-Layer (ML) arrangement of level 1, where fibers are wound around a straight central fiber to form a strand. A second layer of helical fibers can be wound around it, to form a ML arrangement of level 2; adding a third layer one obtains a ML arrangement of level 3. Schemes of this kind can be exploited to produce structural cables based on helically arranged CNTFs. Hereafter, we will consider ML arrangements of level 1 with two, three, four, and seven fibers (referred to as 2-wire, 3-wire, 4-wire, and

7-wire strands, respectively), as well as ML cables composed of a number $M \gg 1$ of layers, providing analytical formulas to estimate their mechanical properties .

3.1. N-wire strand

Let us consider a strand made of helical fibers of radius R_f and length L_f, which are wound around a cylinder of radius R_0, so that the minimum distance between their axis and the axis of the strand is equal to $R = R_0 + R_f$. As shown in Figure 5, a *2-wire strand* is a double helix of two fibers, for which $R_0 = 0$ and $R = R_f$. In *3-wire strand* $R = 2/\sqrt{3}\, R_f$, whereas in a *4-wire strand* $R = \sqrt{2} R_f$. Finally, a *7-wire strand* is composed of six fibers twisted around a central straight fiber, such that $R_0 = R_f$ and $R = 2\, R_f$. The manufacturing and the mechanical properties of basic arrangements of this kind are now discussed.

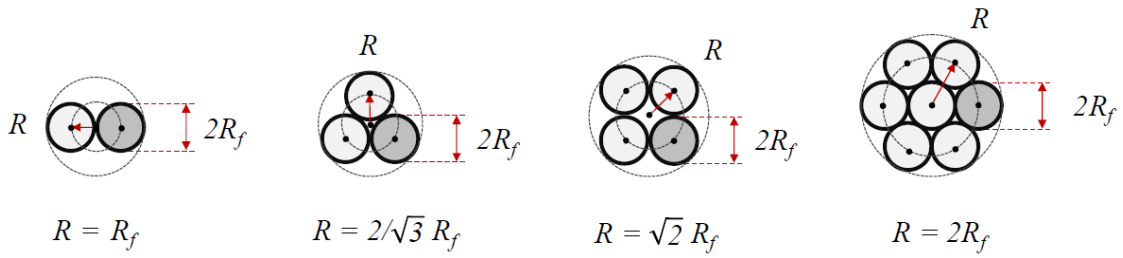

Figure 5: Schematic cross-sectional view of strands of fibers: 2-wire strand, 3-wire strand, 4-wire strand, 7-wire strand, and the corresponding radius R for the helical configuration.

3.1.1. Manufacturing

The way in which SS-CNTFs can be organized in a strand presents similarities with the manufacturing of hemp ropes: first, individual fibers are pulled and pre-twisted; secondly, they are brought closer and wound together, in such a way that the sectional pre-twist turns into the tortuosity of the centreline. The relationship between cross-sectional twist θ' and tortuosity-induced twist $\varphi' \sin\gamma$ has been discussed in Section (2.3). A torsion-free state is achieved under the condition (2.26), when the pre-twist

θ' for the straight fiber is transformed into the tortuosity $\varphi' \sin\gamma$ for the helical fiber. For a helix of radius R, we have

$$\theta' = -\frac{\sin 2\gamma}{2R}\,. \tag{3.30}$$

This equation can be used for design purposes, since it provides the pre-twist to obtain the desired helical configuration or, vice versa, the slope γ that corresponds to a prescribed pre-twist θ'.

Let us suppose that a strand has been manufactured: each fiber of cross-sectional radius R_f is now arranged according to a helix of length L_f, radius R, and slope γ. Let $L = L_f \sin\gamma$. In the parametric representation (2.18), then φ spans the angle α, with $\alpha R = L_f \cos\gamma$. This will be referred to as the *reference configuration* of the strand. Figure 6(a) represents the longitudinal view, the cross section and the helix parameters for the particular case of a 7-wire strand.

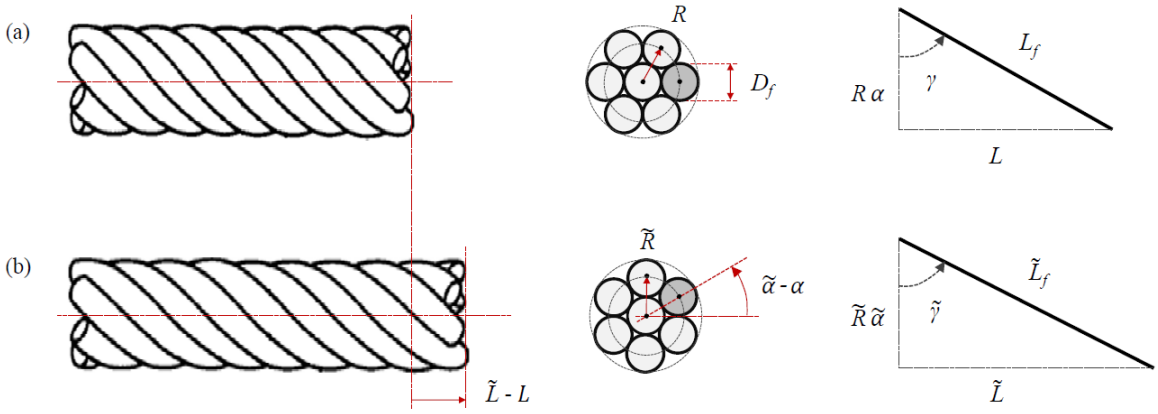

Figure 6: A 7-wire strand: longitudinal view, cross section and geometric parameters of the helix in the (a) reference configuration and in the (b) strained configuration.

In this configuration, two sockets are applied at the strand ends, in such a way that the relative position of the fibers remains fixed and rotation of their end sections is

prevented. At this stage a system of forces are applied at the ends of the strand, which are equipollent to an axial force and a twisting moment. Because of the presence of the sockets, all fibers are uniformly strained and negligible friction forces between them come up. Therefore, the actual (deformed) state of the fiber can be again obtained with reference to the model problem represented in Figure 4(b): the helical fibers deform into a new helix, described by the new parameters $\widetilde{L}_f$, $\widetilde{L}$, $\widetilde{R}$, $\widetilde{\alpha}$, $\widetilde{\gamma}$, indicated in Figure 6(b). Here, we are considering that the distance R may vary to $\widetilde{R}$ because of the lateral contraction of the fibers associated with the Poisson's ratio, which will be considered by using the approximation stated by (2.13). The angle θ' is not varied because the sockets prevent the rotations of the end sections.

The peculiarity of the 7-wire strand is that there is a straight central fiber which remains straight in the deformation, though elongated and twisted. This needs to be taken into account while evaluating the mechanical properties of the strand. Instead, in 2-wire, 3-wire, 4-wire strands there is no central fiber to consider.

3.1.2. Effective mechanical properties

The *macroscopic* strain in a straight strand is described by the axial strain ε (extension of the centreline) and the twist rate β (relative torsional rotation of the end sections per unit axial length), defined as

$$\varepsilon = \frac{\widetilde{L} - L}{L}\,, \tag{3.31a}$$

$$\beta = \frac{\widetilde{\alpha} - \alpha}{L}\,. \tag{3.31b}$$

When there is a central fiber, as in a 7-wire strand, its axial strain and twist rate are assumed to coincide with ε and β, respectively. The helical fibers modify their geometry according to $\Delta L_f = \widetilde{L}_f - L_f$, $\Delta L = \widetilde{L} - L$, $\Delta R = \widetilde{R} - R$, $\Delta\alpha = \widetilde{\alpha} - \alpha$, $\Delta\gamma = \widetilde{\gamma} - \gamma$, whereas the sectional twist θ' in each fiber remains constant. These

geometric parameters, as well as a schematic of the varied configuration of the strand, are represented in Figure 6.

In addition, we recall from Section 3.1.1 that the axial strain in the fibers is nil in the strand reference configuration, and so is the torsion curvature of the helical fibers, which are in a torsion-free state as per (2.26), but the bending curvature is not. Its value, in the reference state, will be denoted by $k_{\mathcal{B}_f}^{(0)} = \cos^2\gamma/R$.

Supposing small changes in the configuration, such that $\Delta\alpha$, $\Delta\gamma$, $\varepsilon_f = \Delta L_f/L_f$ and $\Delta L/L$ are infinitesimal of the first order, and neglecting terms of higher order in equations (3.31), one obtains

$$\varepsilon = \frac{(1+\varepsilon_f)\sin\tilde{\gamma} - \sin\gamma}{\sin\gamma} \simeq \varepsilon_f + \frac{\Delta\gamma}{\tan\gamma}\,, \tag{3.32a}$$

$$R\beta = \frac{(R/\tilde{R})(1+\varepsilon_f)\cos\tilde{\gamma} - \cos\gamma}{\sin\gamma} \simeq \frac{\varepsilon_f}{\tan\gamma} - \Delta\gamma - \frac{\Delta R}{R\tan\gamma}\,, \tag{3.32b}$$

where the symbol $\simeq$ denotes up to first order terms, and ΔR accounts for the fibers cross-sectional contraction and is expressed in the form

$$\frac{\Delta R}{R} = -\nu_f\varepsilon_f + \nu_f^*\left(\varepsilon_f - \varepsilon\right), \tag{3.33}$$

with $\nu_f^* = \nu_f/2$ only for a 7-wire strand for which $\varepsilon_f \geq \varepsilon$, $\nu_f^* = 0$ otherwise. The term proportional to ν_f^* in (3.33) accounts for the fact that the cross-sectional contraction of the central fiber of the 7-wire strand may be so high, with respect to the lateral contraction of the surrounding fibers, that the contact is lost. The contact is maintained only when the strain ε_f of the surrounding fibers is higher than the strain ε of the central fiber. This effect is small with respect to $\nu_f\varepsilon_f$ when $\varepsilon_f \simeq \varepsilon$.

By combining equations (3.32)-(3.33), after some algebraic calculations and neglecting higher order terms, one obtains

$$\varepsilon_f = \frac{(\tan^2\gamma - \nu_f^*)\varepsilon + R\beta\tan\gamma}{1+\tan^2\gamma+\nu_f-\nu_f^*}\,, \tag{3.34a}$$

$$\Delta\gamma = \frac{(1+\nu_f)\varepsilon - R\beta\tan\gamma}{1+\tan^2\gamma+\nu_f-\nu_f^*}\tan\gamma\,, \tag{3.34b}$$

$$\frac{\Delta R}{R} = -\frac{(\nu_f\tan\gamma+\nu_f^*)\varepsilon + (\nu_f-\nu_f^*)R\beta\tan\gamma}{1+\tan^2\gamma+\nu_f-\nu_f^*}\,. \tag{3.34c}$$

We can now express the variation of the bending and torsion curvatures of the strand helical fibers, $\Delta k_{\mathcal{B}_f} = \widetilde{k}_{\mathcal{B}_f} - k_{\mathcal{B}_f}^{(0)}$ and $\Delta k_{\mathcal{T}_f} = \widetilde{k}_{\mathcal{T}_f}$ (recall that the reference state is torsion-free, whereas $k_{\mathcal{B}_f}^{(0)} = \cos^2\gamma/R$), in terms of $\Delta\gamma$ and ΔR, in the form

$$\Delta k_{\mathcal{B}_f} = -\frac{\cos^2\gamma}{R}\frac{\Delta R}{R} - \frac{\sin 2\gamma}{R}\Delta\gamma\,, \tag{3.35a}$$

$$\Delta k_{\mathcal{T}_f} = -\frac{\sin\gamma\cos\gamma}{R}\frac{\Delta R}{R} + \frac{\cos 2\gamma}{R}\Delta\gamma\,. \tag{3.35b}$$

This permits to express the strain energy density of a N-wire strand per unit length of its reference axis (the strand reference length is L) as the sum of two contributions, that is, $W = W_0 + W_1$, such that

$$W_0 = \mathcal{I}_c\left[\frac{1}{2}\mathcal{E}_f\varepsilon^2 + \frac{1}{2}\mathcal{T}_f\beta^2\right]\,, \tag{3.36a}$$

$$W_1 = \frac{N-\mathcal{I}_c}{\sin\gamma}\left[\frac{1}{2}\mathcal{E}_f\varepsilon_f^2 + \frac{1}{2}\mathcal{B}_f(k_{\mathcal{B}_f}^{(0)}+\Delta k_{\mathcal{B}_f})^2 + \frac{1}{2}\mathcal{T}_f(\Delta k_{\mathcal{T}_f})^2\right]\,, \tag{3.36b}$$

where $\mathcal{I}_c$ is the indicator of the central fiber, with $\mathcal{I}_c = 1$ if the central fiber is present (7-wire strand), $\mathcal{I}_c = 0$ otherwise, and N is the number of fibers of the N-wire strand. Note that the term W_0 accounts for the energy associated with the straight central fiber, while W_1 represents the contribution of the strand helical fibers.

By combining equations (3.34)-(3.36), it is evident that W can explicitly be expressed in terms of the macroscopic strain measures ε and β. In order to describe the overall

stiffness of the system, what is important is the part of W, hereafter called $W^{(2)}$, which contains the quadratic terms in ε and β. This can be expressed in the form

$$W^{(2)} = \frac{1}{2}\mathcal{E}\varepsilon^2 + \frac{1}{2}\mathcal{T}\beta^2 + \mathcal{X}\varepsilon\beta\,, \tag{3.37}$$

where $\mathcal{E}$ and $\mathcal{T}$ are the effective axial stiffness and torsion stiffness of the strand, while $\mathcal{X}$ accounts for the tension-torsion coupling due to the helical arrangement. Such parameters generally depend on the slope γ of the helical fibers in the arrangement, their diameter D_f, and Poisson's ratio ν_f. The resulting expressions are quite lengthy, but compact formulas can be obtained in two specific limit cases, which we repute of interest for practical applications.

In the first limit case, the cross-sectional contraction of the fiber is neglected: hence $\nu_f = 0$ and, consequently, $\Delta R = 0$. One obtains

$$\frac{\mathcal{E}}{\mathcal{E}_f} = \mathcal{I}_c + (N - \mathcal{I}_c)\left(1 + \frac{\mathcal{B}_f}{\mathcal{E}_f R^2}\frac{\sin^2 2\gamma}{\tan^2\gamma} + \frac{\mathcal{T}_f}{\mathcal{E}_f R^2}\frac{\cos^2 2\gamma}{\tan^2\gamma}\right)\sin^3\gamma\,, \tag{3.38a}$$

$$\frac{\mathcal{T}}{\mathcal{E}_f R^2} = \frac{\mathcal{I}_c\mathcal{T}_f}{\mathcal{E}_f R^2} + (N - \mathcal{I}_c)\left(1 + \frac{\mathcal{B}_f}{\mathcal{E}_f R^2}\frac{\sin^2 2\gamma}{\cot^2\gamma} + \frac{\mathcal{T}_f}{\mathcal{E}_f R^2}\frac{\cos^2 2\gamma}{\cot^2\gamma}\right)\sin\gamma\cos^2\gamma\,, \tag{3.38b}$$

$$\frac{\mathcal{X}}{\mathcal{E}_f R} = (N - \mathcal{I}_c)\left(1 - \frac{\mathcal{B}_f}{\mathcal{E}_f R^2}\sin^2 2\gamma - \frac{\mathcal{T}_f}{\mathcal{E}_f R^2}\cos^2 2\gamma\right)\sin^2\gamma\cos\gamma\,, \tag{3.38c}$$

where, we recall, $R = D_f/2$ in a *2-wire strand*, $R = D_f/\sqrt{3}$ in a *3-wire strand*, $R = D_f/\sqrt{2}$ in a *4-wire strand*, and $R = D_f$ in a *7-wire strand*.

The second limit case is that in which the effect of Poisson's ratio ν_f is considered, but the contribution of the stiffness parameters $\mathcal{B}_f$ and $\mathcal{T}_f$ is neglected. One finds

$$\frac{\mathcal{E}}{\mathcal{E}_f} = \mathcal{I}_c + (N - \mathcal{I}_c)\eta_f^2\sin^3\gamma\,, \tag{3.39a}$$

$$\frac{\mathcal{T}}{\mathcal{E}_f R^2} = \frac{(N - \mathcal{I}_c)\eta_f^2}{(1 - \nu_f^* \cot^2\gamma)^2} \sin\gamma \cos^2\gamma \,, \tag{3.39b}$$

$$\frac{\mathcal{X}}{\mathcal{E}_f R} = \frac{(N - \mathcal{I}_c)\eta_f^2}{1 - \nu_f^* \cot^2\gamma} \sin^2\gamma \cos\gamma \,, \tag{3.39c}$$

where η_f is a dimensionless coefficient that takes the form

$$\eta_f = 1 - \cot^2\gamma \, \frac{\nu_f - (\nu_f - \nu_f^*)\cos^2\gamma}{1 + (\nu_f - \nu_f^*)\cos^2\gamma} \,. \tag{3.40}$$

The trend of η_f is represented in Figure 7 for different values of the slope γ and Poisson's ratio ν_f.

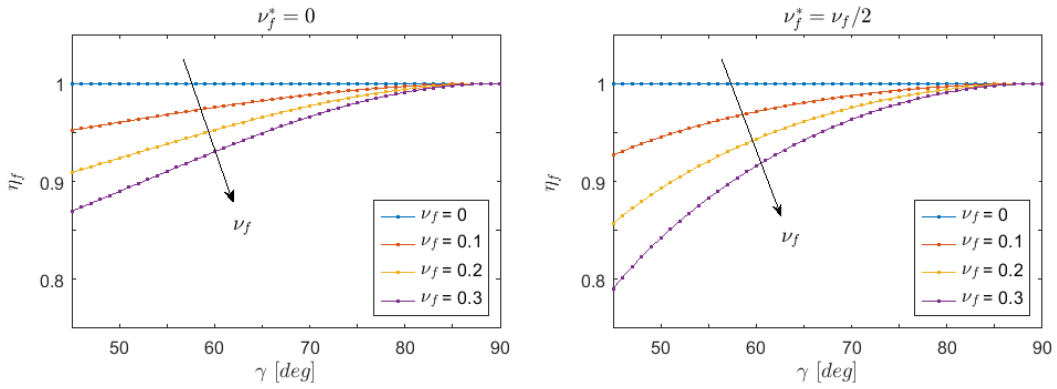

(a) (b)

Figure 7: Coefficient η_f plotted as a function of γ and ν_f: (a) case $\nu_f^* = 0$; (b) case $\nu_f^* = \nu_f/2$.

It is clear that η_f accounts for the decay of the strand stiffness due to the lateral contraction: the straighter the fibers ($\gamma \nearrow$), the less this decay is (recall that straight fibers correspond to $\gamma = 90°$). Observe that the difference between the cases $\nu_f^* = 0$ and $\nu_f^* = \nu_f/2$ is really small: it is less than 1% for $\gamma > 65°$. Assuming $\nu_f^* = 0$ for a 7-wire strand, independently of the value of ε_f with respect to ε, allows to simplify the analytical expressions. Moreover, $\eta_f \in (0.9, 1)$ for $\gamma > 65°$, whatever the value of

ν_f. By setting $\nu_f = 0$ ($\eta_f = 1$), for a geometry of this type, equations (3.39) can be approximated by

$$\frac{\mathcal{E}}{\mathcal{E}_f} = \mathcal{I}_c + (N - \mathcal{I}_c)\sin^3\gamma\,, \tag{3.41a}$$

$$\frac{\mathcal{T}}{\mathcal{E}_f R^2} = (N - \mathcal{I}_c)\sin\gamma\cos^2\gamma\,, \tag{3.41b}$$

$$\frac{\mathcal{X}}{\mathcal{E}_f R} = (N - \mathcal{I}_c)\sin^2\gamma\cos\gamma\,. \tag{3.41c}$$

In this limit case, the axial stiffness $\mathcal{E}$ scales with the third power of $\sin\gamma$, whereas $\mathcal{T}$ and $\mathcal{X}$ depend on cubic terms in $\sin\gamma$ and $\cos\gamma$.

3.2. Multi-layer arrangement

The mechanical properties of Multi-Layer (ML) cables, of the type represented in Figure 8, can be obtained with the same arguments of section 3.1. In general, the fiber disposal should be as compact as possible. Therefore, although arrangements of any type could be considered, reference will be made to the case in which the layer 0 is a straight central fiber, the layer 1 is composed by 6 helical fibers (as in a 7-wire strand), and the other layers of fibers are successively added.

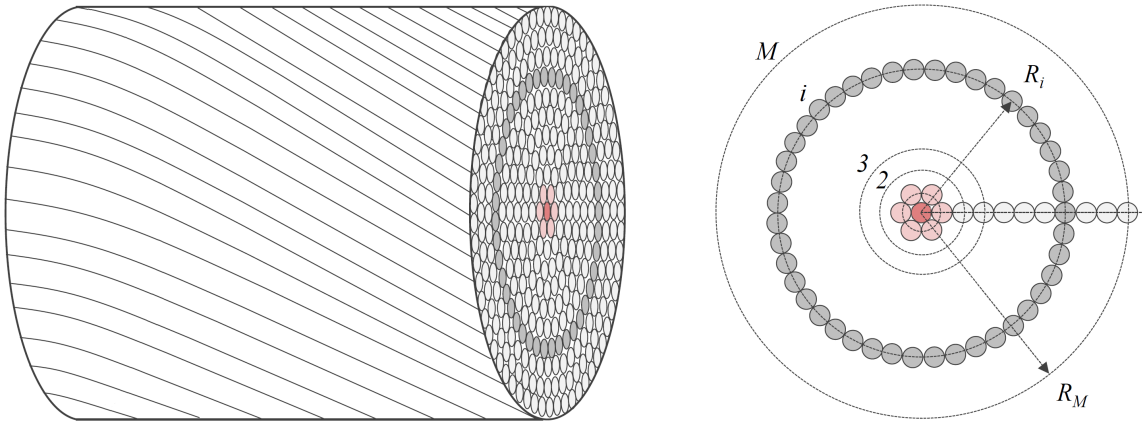

Figure 8: Multi-layer (ML) cable made of helically wound fibers. The red-hatched central fiber is straight (*layer* 0); six fibers, light-red colored, are helically wound around it (*layer* 1); an intermediate layer i, at a distance R_i from the cable axis, is evidenced in grey color; the radius of the outermost layer M of the cable is denoted as R_M.

Manufacturing follows the same procedure illustrated in Section 3.1.1. In the most general case, the fibers shall have variable slope: the expression (3.30) indicates the required pre-twist θ', to be converted in helical tortuosity. Afterwards, sockets are applied at the cable ends. Therefore, in this *reference configuration* of the cable, the fibers are neither stretched nor subject to torsion, though the bending curvature is not nil. In this configuration, R_i denotes the distance of the centroid of a fiber cross-section belonging to the $i-$th layer from the cable axis. With reference to Figure 8, $R_i = 2iR_f$ for $i = 1 \dots M$, where M is the total number of layers.

The energy density function W per unit length of the cable is expressed as the sum of the contribution W_i of the various layers i, for $i = 1 \dots M$, in the form

$$W = W_0 + W_1 + ... + W_M = W_0 + \sum_{i=1}^{M} W_i \,. \tag{3.42}$$

The i-th layer is formed by m_i fibers of slope γ_i, with m_i approximatively equal to the

number of arcs of length $2R_f$ that are contained in a circle of radius $R_i = 2iR_f$, i.e., $m_i \simeq 2i\pi$. This is in general not an integer number, but it can be conventionally used in the following expressions, with good approximation when the cable is composed of a great number of fibers. The term W_0 accounts for the strain energy of the straight central fiber, and it is given by (3.36a) with $\mathcal{I}_c = 1$. The strain energy density of the other layers can be expressed in terms of the strain measures ε and β, as done in Section 3.1.2 for the first layer of a 7-wire strand.

Specifically, the *quadratic* part $W_i^{(2)}$ of the energy density associated with the i-th layer, which dictates the *stiffness* properties, can be written in a form analogous to (3.37), that is

$$W_i^{(2)} = \frac{1}{2}\mathcal{E}_i\varepsilon^2 + \frac{1}{2}\mathcal{T}_i\beta^2 + \mathcal{X}_i\varepsilon\beta\,, \;\; for\; i = 1\dots M\,, \tag{3.43}$$

where ε and β are the axial extension and twist rate of the ML cable, while $\mathcal{E}_i$, $\mathcal{T}_i$, $\mathcal{X}_i$ are the stiffness parameters of the i-th layer, which depend on the radius R_i, the slope γ_i and Poisson's ratio ν_f. By combining equations (3.42) and (3.43), the quadratic part $W_i^{(2)}$ of the strain energy density of the cable can be expressed in the same general form of equation (3.37), with stiffness parameters $\mathcal{E}$, $\mathcal{T}$, $\mathcal{X}$. Their expression can be derived following the procedure previously described also for the general case of layers with different slopes γ_i.

However, to increase the compactness of the cable, it would be convenient to use the same helical slope for all cable fibers, i.e., $\gamma_i = \gamma$ for $i = 1\dots M$. This assumption, as it will discussed later on, implies that all fibers, independently of the layer they belong to, are equally strained: this justifies our basic assumption that the frictional forces between the fibers are negligible, since their relative slipping would be null. In such case, assuming that $M \gg 1$, so that $R_M \gg R_f$, and neglecting the Poisson's

effect ($\nu_f = 0$), one finds

$$\frac{\mathcal{E}}{\mathcal{E}_f} = \left[1 + 2\ln(2M)\left(\frac{\mathcal{B}_f}{\mathcal{E}_f R_M^2}\frac{\sin^2 2\gamma}{\tan^2\gamma} + \frac{\mathcal{T}_f}{\mathcal{E}_f R_M^2}\frac{\cos^2 2\gamma}{\tan^2\gamma}\right)\right]\pi M^2 \sin^3\gamma\,, \tag{3.44a}$$

$$\frac{\mathcal{T}}{\mathcal{E}_f R_M^2} = \left[1 + 2\left(\frac{\mathcal{B}_f}{\mathcal{E}_f R_M^2}\frac{\sin^2 2\gamma}{\cot^2\gamma} + \frac{\mathcal{T}_f}{\mathcal{E}_f R_M^2}\frac{\cos^2 2\gamma}{\cot^2\gamma}\right)\right]\frac{\pi M^2}{2}\sin\gamma\cos^2\gamma\,, \tag{3.44b}$$

$$\frac{\mathcal{X}}{\mathcal{E}_f R_M} = \left[1 + \frac{3}{4}\left(\frac{\mathcal{B}_f}{\mathcal{E}_f R_M^2}\sin^2 2\gamma + \frac{\mathcal{T}_f}{\mathcal{E}_f R_M^2}\cos^2 2\gamma\right)\right]\frac{2\pi M^2}{3}\sin^2\gamma\cos\gamma\,. \tag{3.44c}$$

The quantities $\mathcal{E}$, $\mathcal{T}$, $\mathcal{X}$, characterizing the effective stiffness of the cable, are evidently proportional to the number of cable fibers and explicitly depend on the fiber stiffness parameters, $\mathcal{E}_f$, $\mathcal{B}_f$, $\mathcal{T}_f$ and, of course, on the slope γ.

Moreover, when the contributions associated with $\mathcal{B}_f$ and $\mathcal{T}_f$ are negligible, i.e., when $\mathcal{B}_f \ll \mathcal{E}_f R_M^2$ and $\mathcal{T}_f \ll \mathcal{E}_f R_M^2$, equations (3.44) provide

$$\frac{\mathcal{E}}{\mathcal{E}_f} = \pi M^2 \sin^3\gamma = N\sin^3\gamma\,, \tag{3.45a}$$

$$\frac{\mathcal{T}}{\mathcal{E}_f R_M^2} = \frac{\pi M^2}{2}\,\sin\gamma\cos^2\gamma = N/2\,\sin\gamma\cos^2\gamma\,, \tag{3.45b}$$

$$\frac{\mathcal{X}}{\mathcal{E}_f R_M} = \frac{2\pi M^2}{3}\,\sin^2\gamma\cos\gamma = 2N/3\,\sin^2\gamma\cos\gamma\,, \tag{3.45c}$$

where $N \simeq \pi M^2$ represents the number of fibers of the cable [2].

Equations (3.45) show an explicit dependence of $\mathcal{E}$, $\mathcal{T}$, $\mathcal{X}$ on the stiffness, number, and arrangement of the cable fibers. Observe that the cable axial stiffness $\mathcal{E}$ is obviously maximized by setting $\gamma = 90°$, corresponding to straight fibers. However, helical fibers are expected to provide cables with superior internal cohesion because of the

[2]The number of fibers of the cable is $N = \sum_{i=1}^{M} m_i \simeq \sum_{i=1}^{M} 2i\pi \simeq \pi M^2$, where $m_i = 2\pi R_i/D_f$, while $M \gg 1$ is the number of layers of the cable.

radial interactions f_{R_i} that take place among the layers, which can be determined by exploiting equation (2.29), as is also discussed in Section 4.3.

4. Results

The results of Section 3.1 for the Basic Arrangement of a N-wire strand, and of Section 3.2 for a Multi-Layer (ML) cable, are now discussed in a parametric analysis with reference to an element under uniaxial traction and null twist ($\beta = 0$). This condition applies to strands/cables used in the most common structural applications.

4.1. Effective axial stiffness of N-wire strands

Consider a strand made of $N = 2, 3, 4, 7$ CNT fibers of diameter D_f, arranged as in Figures 5-6, under the action of the axial load F transmitted by terminal sockets preventing the rotation of the end sections. In the strand reference state the fibers are helically wound with slope γ; when $N = 7$, there is also a central straight fiber.

Referring to the experimental data of [21], the fiber axial stiffness is of the order of $\mathcal{E}_f = 27.5\,\mathrm{N\ mm/mm}$ when the length of the constituent CNTs is $l = 2.21\,\mu\mathrm{m}$; it almost doubles ($\mathcal{E}_f = 54.4\,\mathrm{N\ mm/mm}$) when l increases up to $6.28\,\mu\mathrm{m}$. In all cases, the CNT diameter is $d = 1.5\,\mathrm{nm}$, while the diameter of the CNT fiber is $D_f = 22\,\mu\mathrm{m}$. For what concerns the bending stiffness $\mathcal{B}_f$, from [21] one finds that $\mathcal{B}_f/(\mathcal{E}_f D_f^2)$, to be used in (3.38), ranges in the interval $(0.01, 0.05)$: this justifies why this term may be neglected with respect to the other ones, as done in the limit case of (3.41a). To the best of our knowledge, experimental data of the torsional stiffness $\mathcal{T}_f$ and Poisson's ratio ν_f are not yet available for the fibers. Therefore, we present a parametric analysis where the dimensionless parameters $\mathcal{B}_f/(\mathcal{E}_f D_f^2)$ and $\mathcal{T}_f/(\mathcal{E}_f D_f^2)$ are made to vary in the range $(0, 0.1)$, whereas ν_f takes values in the interval $(0, 0.3)$.

For a 7-wire strand, Figure 9 shows the axial stiffness $\mathcal{E}$ as a function of γ for different values of $\mathcal{B}_f/(\mathcal{E}_f D_f^2)$, $\mathcal{T}_f/(\mathcal{E}_f D_f^2)$ and ν_f. The plotted values are made dimensionless

by considering the ratio between $\mathcal{E}$ and $\mathcal{E}_{ref} = N\mathcal{E}_f$, representing the stiffness of N straight fibers. Figures 10-11 report the results for the other stiffness parameters of the strand to be inserted in (3.37), namely $\mathcal{T}$ and $\mathcal{X}$, with respect to the reference values $\mathcal{T}_{ref} = N\mathcal{E}_f D_f^2/4$ and $\mathcal{X}_{ref} = \sqrt{\mathcal{E}_{ref}\mathcal{T}_{ref}} = N\mathcal{E}_f D_f/2$. Observe that $\mathcal{T}_{ref}$ indicates the torsional stiffness of a beam with compact circular cross-section[3], radius $R = 2R_f = D_f$ and $\nu_f = 0$, whereas $\mathcal{X}_{ref}$ is the geometric mean of $\mathcal{E}_{ref}$ and $\mathcal{T}_{ref}$.

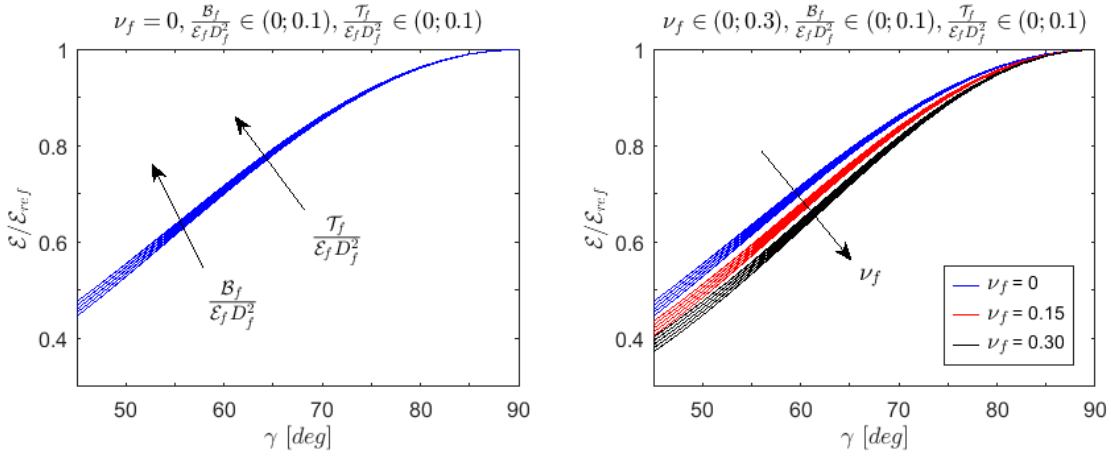

(a) (b)

Figure 9: Axial stiffness $\mathcal{E}$ of a 7-wire strand, made dimensionless with respect to the reference stiffness $\mathcal{E}_{ref} = N\mathcal{E}_f$ of $N = 7$ straight fibers, plotted as a function of the reference slope γ for different values of Poisson's ratio ν_f. Effect of bending stiffness $\mathcal{B}_f/(\mathcal{E}_f D_f^2) \in (0, 0.1)$ and torsional stiffness $\mathcal{T}_f/(\mathcal{E}_f D_f^2) \in (0, 0.1)$ for (a) $\nu_f = 0$, and for (b) $\nu_f \in (0, 0.3)$.

[3]If E_f is the effective Young's modulus of the fibers, for a compact circular section of radius $R = D_f$ one can formally write $N\mathcal{E}_f = E_f \pi R^2$ and, for $\nu_f = 0$, $\mathcal{T}_{ref} = \frac{E_f}{2(1+\nu_f)}\pi R^4/2 = N\mathcal{E}_f D_f^2/4$.

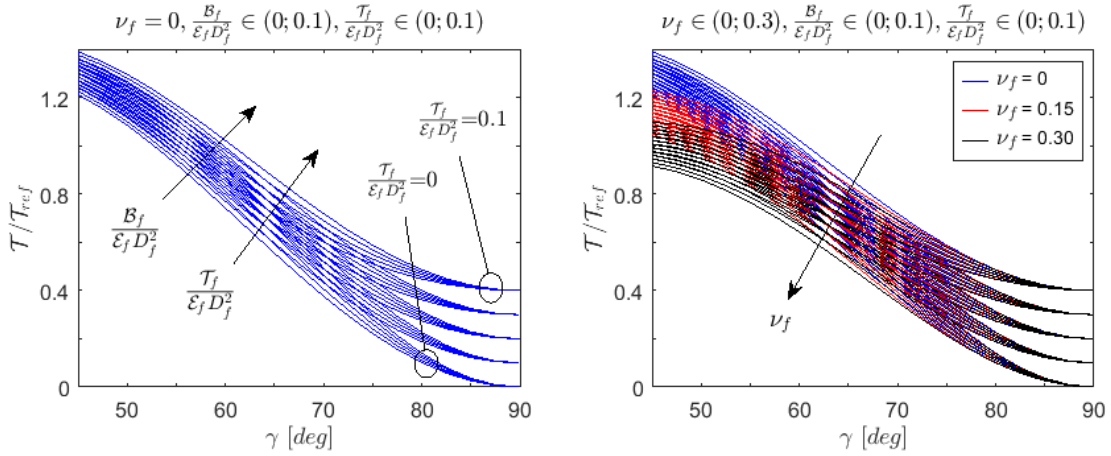

(a) (b)

Figure 10: Torsional stiffness $\mathcal{T}$ of a 7-wire strand, made dimensionless with respect to the reference stiffness $\mathcal{T}_{ref} = N\mathcal{E}_f D_f^2/4$ of a beam with compact circular section of diameter D_f, plotted as a function of the reference slope γ for different values of ν_f. Effect of bending stiffness $\mathcal{B}_f/(\mathcal{E}_f\, D_f^2) \in (0, 0.1)$ and torsional stiffness $\mathcal{T}_f/(\mathcal{E}_f\, D_f^2) \in (0, 0.1)$ for (a) $\nu_f = 0$, and for (b) $\nu_f \in (0, 0.3)$.

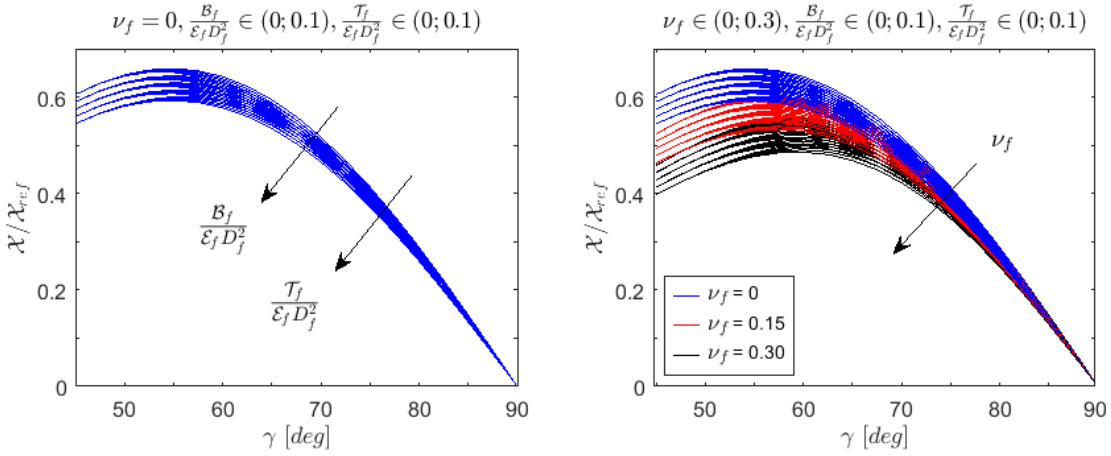

(a) (b)

Figure 11: Coefficient of torsion-extension coupling $\mathcal{X}$ of a 7-wire strand, made dimensionless with respect to the reference value $\mathcal{X}_{ref} = \sqrt{\mathcal{E}_{ref}\mathcal{T}_{ref}} = N\mathcal{E}_f D_f/2$, plotted as a function of the reference slope γ for different values of Poisson's ratio ν_f. Effect of bending stiffness $\mathcal{B}_f/(\mathcal{E}_f\, D_f^2) \in (0, 0.1)$ and torsional stiffness $\mathcal{T}_f/(\mathcal{E}_f\, D_f^2) \in (0, 0.1)$ for (a) $\nu_f = 0$, and for (b) $\nu_f \in (0, 0.3)$.

In general, the axial stiffness of a strand is the mechanical property of greatest interest for its structural applications. From Figure 9, observe that the influence of the fiber bending stiffness $\mathcal{B}_f$ and torsional stiffness $\mathcal{T}_f$ on the strand axial stiffness $\mathcal{E}$ is very small, almost negligible for $\gamma > 70°$, and that the effect of the fiber Poisson's ratio ν_f is very mild, especially for $\gamma > 70°$. Similar remarks are valid for the torsional stiffness $\mathcal{T}$ and for the coefficient of torsion-extension coupling $\mathcal{X}$ of the strand, reported in Figures 10 and 11, although their dependence on the fiber mechanical properties ($\mathcal{B}_f$, $\mathcal{T}_f$, ν_f) is stronger than that of the axial stiffness $\mathcal{E}$.

Considering only the contribution of the fiber axial stiffness $\mathcal{E}_f$ in the strand strain energy, it is possible to derive a simple analytical formula for the strand axial stiffness $\mathcal{E}$ which, for the generic case of a N-wire strand, takes the form

$$\frac{\mathcal{E}}{N\mathcal{E}_f} = \frac{\mathcal{I}_c}{N} + \left(1 - \frac{\mathcal{I}_c}{N}\right) \sin^3 \gamma \,, \tag{4.1}$$

where, again, $\mathcal{I}_c$ is the indicator of the central fiber introduced in Section 3.1.2 in equation (3.36). The effect of the fiber Poisson's ratio on the strand axial stiffness can be accounted for by multiplying the second addend on the right hand term of equation (4.1) by η_f^2, with η_f calculated from (3.40) by setting $\nu_f^* = 0$.

We conclude this section by showing comparisons between the results of our model (labelled MDR in Figures 12-14) and those obtainable with models originally developed for metallic wire strands, such as those proposed by Hruska (HR), Mc-Connel and Zemke (MZ), Labrosse (LB), Sathikh (SA) and Foti and Martinelli (FM), mentioned in recent review articles [38, 39], all characterized by a symmetric extension-torsion stiffness matrix. The comparison is in terms of the stiffness parameters $\mathcal{E}$, $\mathcal{T}$, $\mathcal{X}$ of the strand. We recall that the HR model is based on the concept of purely tensile wires and does not account for the fiber bending/torsion stiffness and Poisson's ratio. The

MZ model is obtained by adding to the torsional stiffness considered in HR the sum of the torsional stiffness of all the helical wires of the strand. With respect to the MZ model, the LA approach also considers the effect of the bending stiffness of the helical fibers in the calculation of the overall torsional stiffness of the strand. The influence of the bending/torsion stiffness of the fibers on the overall stiffness parameters of the strand is accounted for in the SA model, but the fiber cross-sectional contraction is again neglected. Poisson's effect is considered by Foti and Martinelli (FM), who, however, do not account for the influence of the fiber bending/torsion stiffness on the strand stiffness parameters $\mathcal{E}$ and $\mathcal{X}$. On the other hand, the model proposed here (MDR) accounts for the influence of all the stiffness parameters at the fiber level ($\mathcal{E}_f$, $\mathcal{T}_f$, $\mathcal{X}_f$) and the Poisson's ratio (ν_f).

Figure 12 shows the results for the strand axial stiffness $\mathcal{E}$, whereas Figures 13 and 14 refer to the torsional stiffness $\mathcal{T}$ and to the coefficient of torsion-extension coupling $\mathcal{X}$, respectively. Figures 12-14(a) correspond to the case of vanishing Poisson's ratio ($\nu_f = 0$), whereas Figures 12-14(b) are for $\nu_f = 0.3$. The labels indicate the considered models, according to the nomenclature presented before; the number 0 or 1, which complements each label, corresponds to the value chosen for the fiber parameters $\mathcal{B}_f/(\mathcal{E}_f\, D_f^2)$ and $\mathcal{T}_f/(\mathcal{E}_f\, D_f^2)$, both equal either to 0 (label number 0, color blue) or 0.1 (label number 1, color red). We remark that, in this work, we do not consider the effects associated with the contact deformation of the wires, their plastic behavior and frictional interactions [30, 44]. Therefore, the contact compliance parameter of the FM model, denoted as C_n in [39], has been set equal to 0 for the examples shown in Figures 12-14.

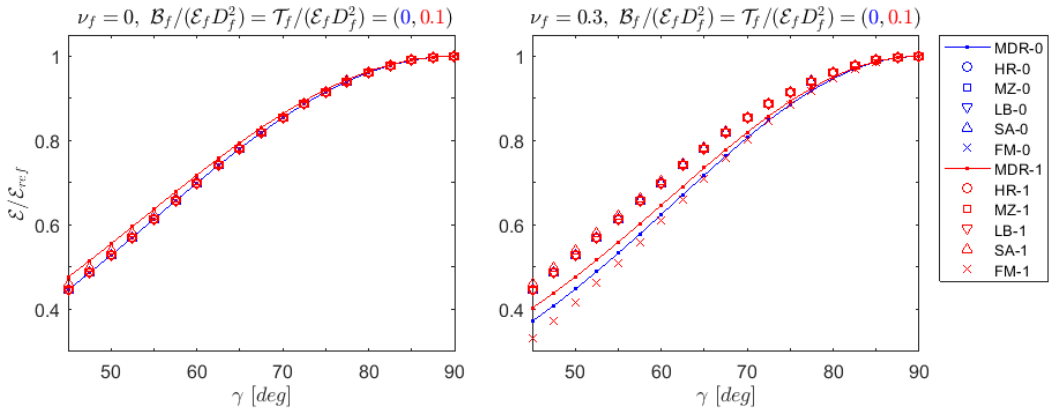

(a) (b)

Figure 12: Axial stiffness $\mathcal{E}$ of a 7-wire strand, made dimensionless with respect to $\mathcal{E}_{ref} = N\mathcal{E}_f$, plotted as a function of γ. Comparison between the proposed model (MDR) and the models by Hruska (HR), Mc-Connel and Zemke (MZ), Labrosse (LB), Sathikh (SA) and Foti and Martinelli (FM), for stiffness parameters $\mathcal{B}_f/(\mathcal{E}_f\, D_f^2)$ and $\mathcal{T}_f/(\mathcal{E}_f\, D_f^2)$ both either equal to 0 (label number 0, blue marks) or 0.1 (label number 1, red marks). Different values of the fiber Poisson's ratio: (a) $\nu_f = 0$ and (b) $\nu_f = 0.3$.

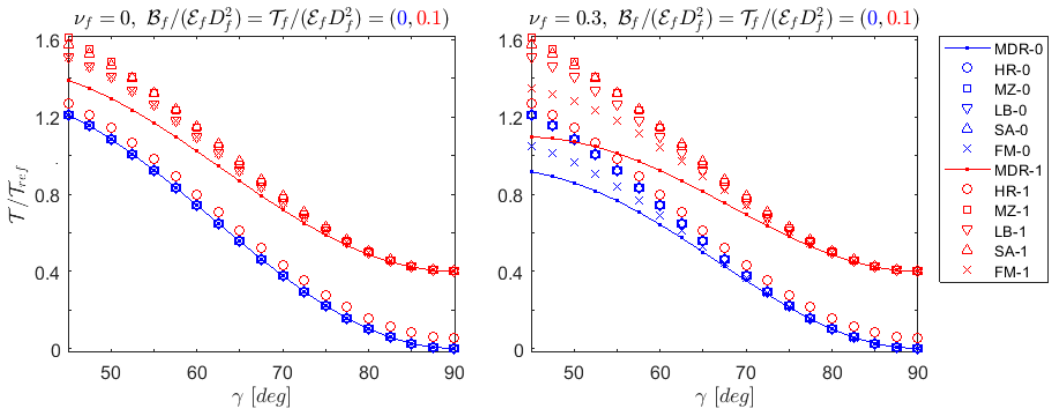

(a) (b)

Figure 13: Torsional stiffness $\mathcal{T}$ of a 7-wire strand, made dimensionless with respect to $\mathcal{T}_{ref} = N\mathcal{E}_f D_f^2/4$, plotted as a function of γ. Comparison between the proposed model (MDR) and the models by Hruska (HR), Mc-Connel and Zemke (MZ), Labrosse (LB), Sathikh (SA) and Foti and Martinelli (FM), for stiffness parameters $\mathcal{B}_f/(\mathcal{E}_f\, D_f^2)$ and $\mathcal{T}_f/(\mathcal{E}_f\, D_f^2)$ both either equal to 0 (label number 0, blue marks) or 0.1 (label number 1, red marks). Different values of the fiber Poisson's ratio: (a) $\nu_f = 0$ and (b) $\nu_f = 0.3$.

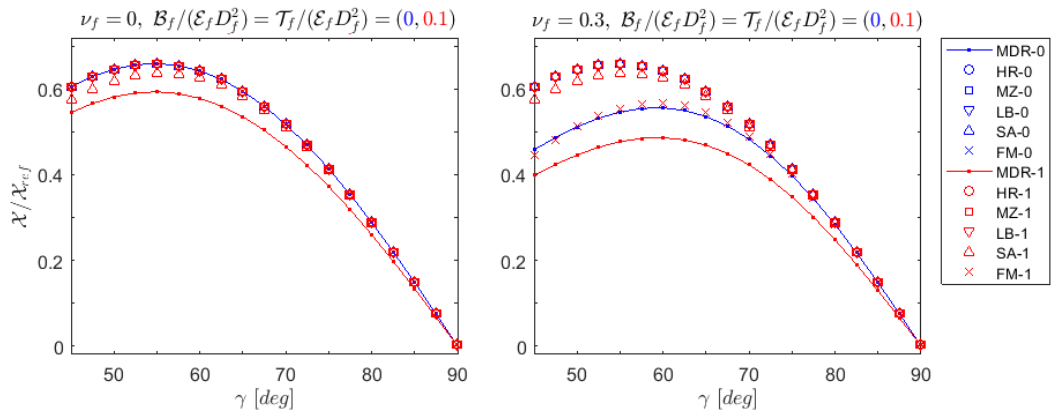

(a) (b)

Figure 14: Torsion-extension coupling coefficient $\mathcal{X}$ of a 7-wire strand, made dimensionless with respect to $\mathcal{X}_{ref} = N\mathcal{E}_f D_f/2$, plotted as a function of γ. Comparison between the proposed model (MDR) and the models by Hruska (HR), Mc-Connel and Zemke (MZ), Labrosse (LB), Sathikh (SA) and Foti and Martinelli (FM), for stiffness parameters $\mathcal{B}_f/(\mathcal{E}_f\, D_f^2)$ and $\mathcal{T}_f/(\mathcal{E}_f\, D_f^2)$ both either equal to 0 (label number 0, blue marks) or 0.1 (label number 1, red marks). Different values of the fiber Poisson's ratio: (a) $\nu_f = 0$ and (b) $\nu_f = 0.3$.

From Figure 12, it is clear that all the models provide almost the same axial stiffness $\mathcal{E}$ for $\nu_f = 0$, regardless of the value of the fiber bending/torsional stiffness, provided that the dimensionless parameters $\mathcal{B}_f/(\mathcal{E}_f\, D_f^2)$ and $\mathcal{T}_f/(\mathcal{E}_f\, D_f^2)$ are in the interval $(0, 0.1)$. The models that account for the Poisson's effect are our MDR and the FM, but the results from the other approaches have been juxtaposed for the sake of comparision. Their predictions in terms of $\mathcal{E}$ are almost coincident for $\gamma > 70°$; the differences are within 10% for $\gamma \in (45°, 90°)$. It is important to recall that the FM model does not consider the effect of the fiber bending/torsional stiffness. In any case, our MDR model shows that the contribution of $\mathcal{B}_f$ and $\mathcal{T}_f$ is very small even for $\nu_f = 0.3$, and becomes negligible for $\gamma > 70°$.

The differences among the various models are more evident in terms of torsional stiffness $\mathcal{T}$ (Figure 13) and torsion-extension coupling coefficient $\mathcal{X}$ (Figure 14). For

$\nu_f = 0$, all models, apart from HR, provide results very close one another for $\gamma > 70°$, at least for the considered range of variation of $\mathcal{B}_f$ and $\mathcal{T}_f$. The Poisson's effect can again be evaluated only by the MDR and the FM models. Its influence on $\mathcal{T}$ is very small if $\gamma > 70°$, while the effect on $\mathcal{X}$ is higher and becomes mild only for $\gamma > 80°$. Noteworthy differences arise between these two models for lower values of γ and non-vanishing values of the Poisson's ratio (case $\nu_f = 0.3$). In general, the FM model overestimate the parameters $\mathcal{T}$ and $\mathcal{X}$ with respect to the MDR model.

This comparison illustrates the capability of the various models to account for the influence of the fiber stiffness parameters and Poisson's ratio on the properties of the strand. In any case, only an experimental campaign, which is the next step in our planned activities, can corroborate the theoretical findings discussed here and the effectiveness of the proposed modeling approach in the prediction of the mechanical properties of strands made of helically wound CNT fibers.

4.2. Effective axial stiffness of multi-layer cables

Consider a ML cable composed of $N \gg 1$ CNT fibers of diameter D_f, arranged in M layers helically wound as per Figure 8, all with the same helical slope γ in the reference state. The cable ends are again constrained by two terminal sockets, which transmit the axial load F to the cable but prevent the sectional rotation. The first two layers of this cable coincide with a 7-wire strand. The cable is made of the same SS-CNTFs considered in the previous section. The parametric analysis considers the same variations $\mathcal{B}_f/(\mathcal{E}_f D_f^2) \in (0, 0.1)$, $\mathcal{T}_f/(\mathcal{E}_f D_f^2) \in (0, 0.1)$ and $\nu_f \in (0, 0.3)$.

For a ML cable made of $N = 3.1 \cdot 10^4$ fibers arranged in $M = 100$ layers, Figures 15-17 respectively report the cable stiffness parameters, $\mathcal{E}$, $\mathcal{T}$, $\mathcal{X}$, as functions of γ, for different values of $\mathcal{B}_f/(\mathcal{E}_f D_f^2)$, $\mathcal{T}_f/(\mathcal{E}_f D_f^2)$, ν_f, with respect to the reference parameters $\mathcal{E}_{ref} = N\mathcal{E}_f$, $\mathcal{T}_{ref} = N\mathcal{E}_f R_M^2/4$, $\mathcal{X}_{ref} = N\mathcal{E}_f R_M/2$, where $R_M = MD_f$ is the radius of the outermost layer of the cable, as per Figure 8. These parameters are

the counterparts of those considered for the 7-wire strand in Section 4.1.

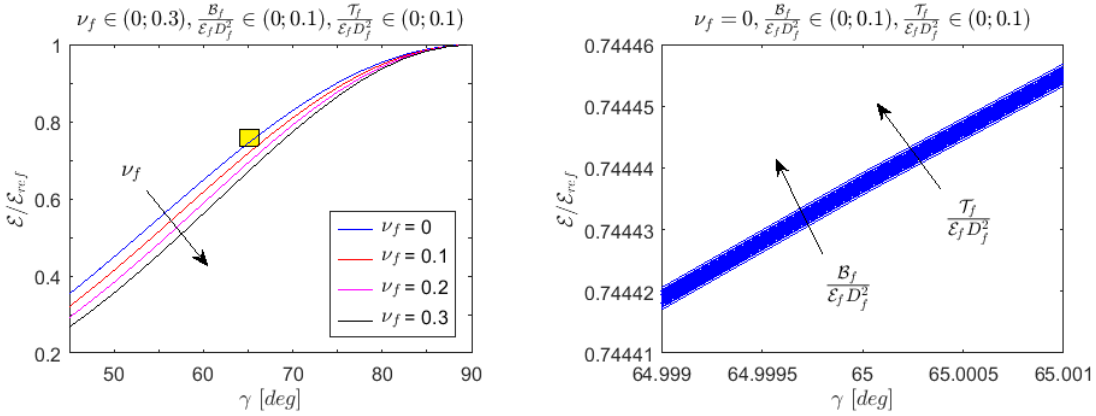

(a) (b)

Figure 15: Axial stiffness $\mathcal{E}$ of a ML cable composed of $N = 3.1 \cdot 10^4$ fibers arranged in $M = 100$ layers, made dimensionless with respect to the reference stiffness $\mathcal{E}_{ref} = N\mathcal{E}_f$, plotted as a function of the reference helical slope γ. (a) Varying bending stiffness ($\mathcal{B}_f/(\mathcal{E}_f\, D_f^2) \in (0, 0.1)$), torsional stiffness ($\mathcal{T}_f/(\mathcal{E}_f\, D_f^2) \in (0, 0.1)$) and Poisson's ratio ($\nu_f \in (0, 0.3)$) of the fiber; (b) magnification of the yellow-hatched rectangle corresponding to $\nu_f = 0$.

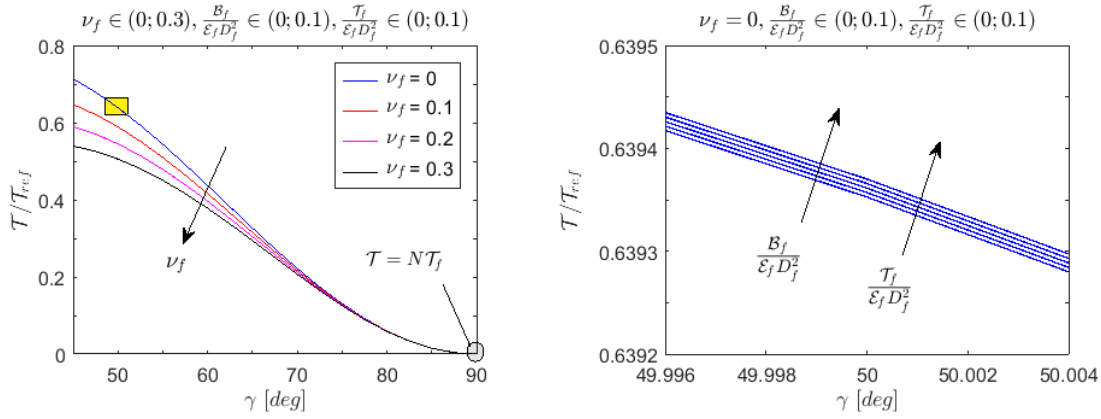

(a) (b)

Figure 16: Torsional stiffness $\mathcal{T}$ of a ML cable composed of $N = 3.1 \cdot 10^4$ fibers arranged in $M = 100$ layers, made dimensionless with respect to the reference stiffness $\mathcal{T}_{ref} = N\mathcal{E}_f R_M^2/4$, plotted as a function of the reference helical slope γ. (a) Varying bending stiffness $(\mathcal{B}_f/(\mathcal{E}_f\, D_f^2) \in (0, 0.1))$, torsional stiffness $(\mathcal{T}_f/(\mathcal{E}_f\, D_f^2) \in (0, 0.1))$ and Poisson's ratio $(\nu_f \in (0, 0.3))$ of the fiber; (b) magnification of the yellow-hatched rectangle corresponding to $\nu_f = 0$.

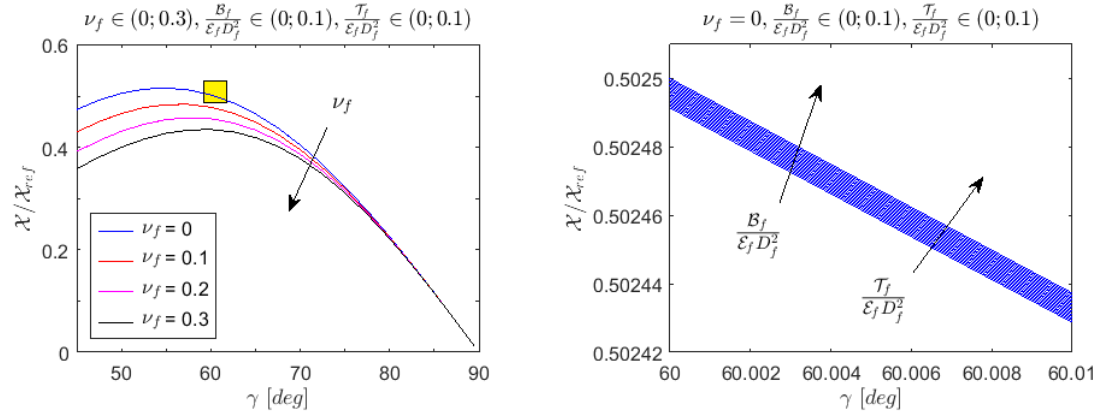

(a) (b)

Figure 17: Coefficient of torsion-extension coupling $\mathcal{X}$ for a ML cable composed of $N = 3.1 \cdot 10^4$ fibers arranged in $M = 100$ layers, made dimensionless with respect to the reference value $\mathcal{X}_{ref} = N\mathcal{E}_f R_M/2$, plotted as a function of the reference helical slope γ. (a) Varying bending stiffness $(\mathcal{B}_f/(\mathcal{E}_f\, D_f^2) \in (0, 0.1))$, torsional stiffness $(\mathcal{T}_f/(\mathcal{E}_f\, D_f^2) \in (0, 0.1))$ and Poisson's ratio $(\nu_f \in (0, 0.3))$ of the fiber; (b) magnification of the yellow-hatched rectangle corresponding to $\nu_f = 0$.

Although the considered case corresponds to a particular number N of fibers, the trend is similar when N is very large. Observe that bending and torsional stiffness of the fibers have a negligible effect on the cable stiffness and also the Poisson's ratio provides a limited influence, especially for $\gamma > 65°$. Therefore, one can again approximate the dependence of $\mathcal{E}$ on the mechanical properties and arrangement of the constituent CNTFs via equation (4.1), as for the case of the strand analyzed in the previous Section.

4.3. Indicators of strain and stress in strands and cables

The helical fibers of a strand/cable under a uniaxial tensile force F and null twist rate β undergo a tensile force $\mathcal{E}_f\varepsilon_f$ and a strain ε_f, which depends upon the strain ε of the strand/cable. Specifically, expressing ε as the ratio between the force F and the axial stiffness $\mathcal{E}$ (which has been determined in Sections 4.1 and 4.2 for the strand and ML cable, respectively), the value of ε_f can be obtained via equation (3.34a) as a function of the reference slope γ, which in the present case is the same for all the cable layers. Observe that for the considered cases $\nu_f^* = 0$. Moreover, since $\beta = 0$, the dependence upon the radius R does not come into play: hence, all fibers undergo the same tensile stress, independently of the layer they belong to in the ML cable.

The proposed model can also be applied to ML cables composed by fibers whose slope differs from layer to layer. Closed form expressions could be obtained for each layer relying on equations (3.42)-(3.43) introduced in the first part of Section 3.2: the cable response would result from the superposition of the contributions of the various layers. However, in this case, fibers belonging to different layers would not be equally strained. Two issues thus arise. First, we anticipate the relative slipping between the layers, but in our model we neglect the frictional contact between the fibers, since the assumed particular geometry implies that they are equally strained. Second, we expect the cable response to depend on the boundary conditions at the

ends of the cable. If a socket constrains all the layers to deform macroscopically in the same way in the axial direction of the cable, one could calculate the state of stress in each layer via kinematic compatibility conditions, assuming that the relative slipping is negligible. Alternatively, if the layers are not constrained at the end sections, a criterion is needed to determine the load that it is borne by each layer, taking into account their frictional contact. The definition of such a criterion requires further studies, to be considered in subsequent works. Here, the analysis is limited to ML cables composed by fibers with the same slope γ.

Figure 18 shows the dimensionless parameter $(\mathcal{E}_f \varepsilon_f)/(F/N)$ associated with the tensile force in the helical fibers as a function of the slope γ. This parameter indicates the tensile force in the fiber with respect to F/N, which represents the tensile force if all the fibers were straight. Recall that the particular assumed geometry, according to which γ is the same for all the fibers, implies that the fibers are equally stressed. The graphs demonstrate that the dependence upon the bending stiffness $(\mathcal{B}_f/(\mathcal{E}_f\, D_f^2) \in (0, 0.1))$ and the torsional stiffness $(\mathcal{T}_f/(\mathcal{E}_f\, D_f^2) \in (0, 0.1))$ of the cable fibers is certainly negligible. The influence of the fiber Poisson's ratio ν_f is very limited, being less than 5% for $\gamma > 65°$.

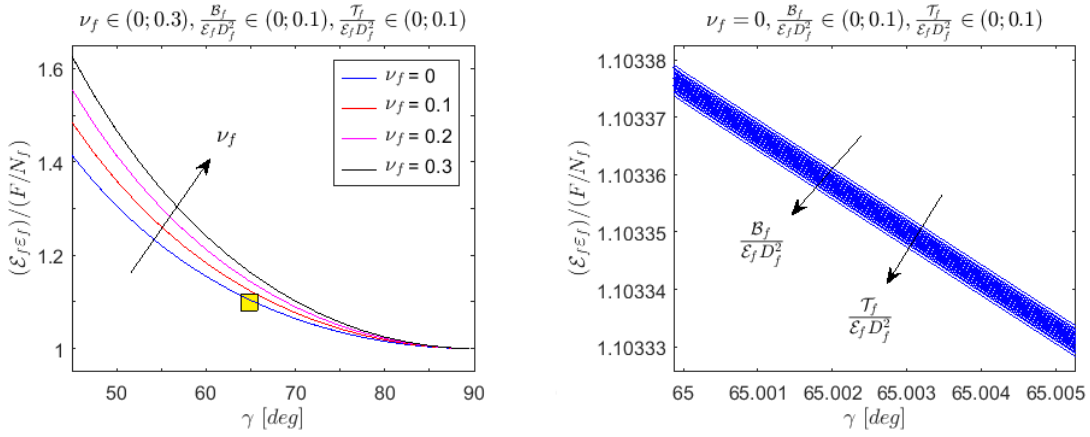

(a) (b)

Figure 18: Normalized tensile force parameter $(\mathcal{E}_f \varepsilon_f)/(F/N)$ in each fiber as a function of the reference slope γ. (a) Effect of varying bending stiffness $(\mathcal{B}_f/(\mathcal{E}_f\, D_f^2) \in (0, 0.1))$ and torsional stiffness $(\mathcal{T}_f/(\mathcal{E}_f\, D_f^2) \in (0, 0.1))$ of the fiber, for different values of the Poisson's ratio $\nu_f \in (0, 0.3)$; (b) magnification of the yellow-hatched rectangle corresponding to $\nu_f = 0$.

For a ML cable there is another stress parameter of paramount importance, which is associated with the radial interaction among the cable layers. As indicated in the microstructural model outlined in Section 2.1, a pressure exerted at right angle with respect to the fiber axis can improve the bond between the lateral surfaces of the CNTs forming the fibers. Moreover, in a ML arrangement the transversal forces compress the fibers together: if a fiber accidentally breaks at a certain section of the cable, the frictional forces associated with the compressive forces allow to re-establish the load-bearing capacity of the broken fiber at a certain distance from the breaking point. This distance, usually referred to as the *bond length* or *anchor length*, is equal to the tensile force in the cable divided by the longitudinal frictional forces per unit length, which depend on the lateral compressions through the friction coefficient. In a cable made up of many fibers, it is unlikely that all of them will break in the same cable section. Consequently, a series of fiber failures, occurring at different sections

spaced at a distance greater than the bond length, does not compromise the overall bearing capacity of the cable. In other words, the *resilience* of the cable can be greatly enhanced by the radial interaction among the fibers.

The previous considerations are to be considered at a qualitative level; as far as we know, this topic has no references in the technical literature. Pending further studies that lead to a quantitative evaluation of the effects, we believe it is useful to propose a semi-empirical analysis, with the aim of posing the problem and stimulating further research, both at an experimental and theoretical level.

The radial forces per unit length f_R, which correspond to the constraint reaction of the cylinder in the model problem of Figure 4(b), can be evaluated via equation (2.29). For a ML cable composed of M layers, the radial compressive forces that are exerted on each fiber of the i-th layer, of radius R_i, can be approximately[4] evaluated by summing up all the actions that are exerted on this layer by the layers $j = i{+}1, \dots, M$. Recall that $R_j = j\, D_f$ and that in the j-th layer the number of fibers is approximately $2\pi R_j/D_f = 2\pi j$. Since it has been previously demonstrated that the axial force $\mathcal{E}_f \varepsilon_f$ is the same in each fiber, from (2.29) the resultant of the radial forces per unit length F_{R_i} on a fiber of the i-th layer is, for $M > i$,

$$F_{R_i} = \sum_{j=i+1}^{M} f_{R_j} \frac{2\pi R_j/D_f}{2\pi R_i/D_f} = \frac{R_M - R_i}{D_f R_i} \mathcal{E}_f \varepsilon_f \cos^2 \gamma \,, \tag{4.2}$$

and, consequently,

[4]The approximation consists in the fact that, by summing up all the contributions, we are neglecting the circumferential stiffness of each layer of fibers, which may shield the radial pressure transmitted on the inner layers by the outer layers. The evaluation of this effect goes beyond the scope of this article.

$$\frac{F_{R_i} D_f}{\mathcal{E}_f \varepsilon_f} = \cos^2 \gamma \left(\frac{R_M}{R_i} - 1 \right). \tag{4.3}$$

Figure 19 shows the dimensionless parameter $(F_{R_i} D_f)/(\mathcal{E}_f \varepsilon_f)$ as a function of the reference slope γ of the helical fibers and of the radius R_i of the i-th layer for a ML cable made of $M = 100$ layers ($R_M = 100 D_f$). Kept fixed the tensile force $\mathcal{E}_f \varepsilon_f$ in the cable, it is evident that F_{R_i} increases by reducing γ and that the inner layers are more compressed than the external one. Conversely, recall from Section 4.2 that the effective axial stiffness increases with γ.

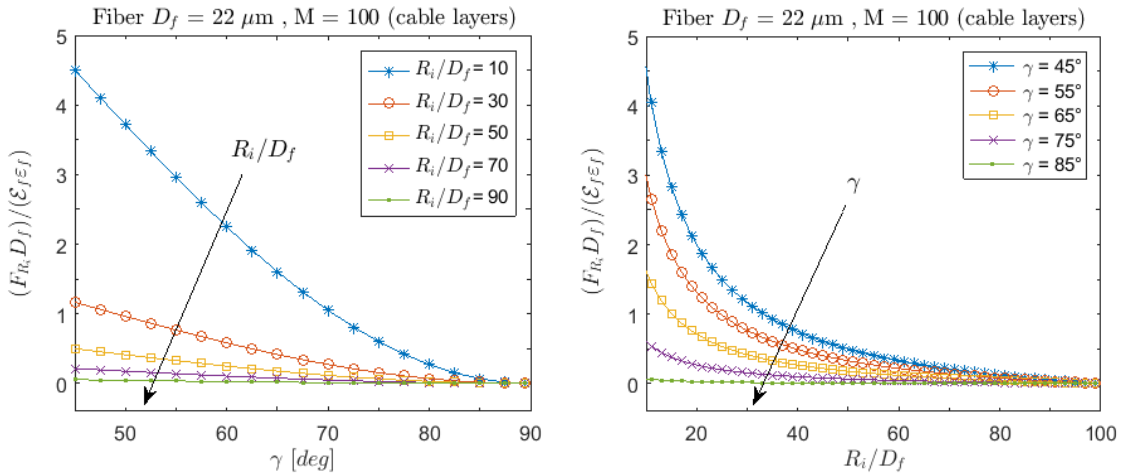

(a) (b)

Figure 19: Dimensionless parameter $(F_{R_i} D_f)/(\mathcal{E}_f \varepsilon_f)$, where $\mathcal{E}_f \varepsilon_f$ is the fiber tensile force, describing the radial forces (F_{R_i} exerted on the i-th layer of a ML cable composed of $M = 100$ layers ($R_M = 100 D_f$), plotted as a function of: (a) the reference slope γ of the helical fibers at various layers R_i; (b) the radius R_i of the i-th layer, normalized with respect to D_f for various values of γ.

Therefore, it is expected that there is a value of the reference slope γ that represents an optimal compromise between the strength and stiffness of the ML cable for a specific application. Determining such a value requires a precise definition of the

tensile strength of a CNTF as a function of the transversal forces acting on it, but this will be the subject of future research.

Although further studies are certainly needed for a quantification of the effect, for illustrative purposes suppose that the strength σ_c of a wound CNTF can be expressed in the form $\sigma_c = \sigma + \lambda_\sigma F_{R_i}/D_f$, where σ is the tensile strength for an isolated CNTF, and λ_σ is a dimensionless coefficient that characterizes the improved strength consequent to the compressive radial forces F_{R_i}. It is of interest to consider the gain in terms of σ_c/σ, which can be expressed in the form

$$\frac{\sigma_c}{\sigma} = 1 + \lambda_\sigma \frac{F_{R_i} D_f}{\mathcal{E}_f \varepsilon_f} \frac{\mathcal{E}_f \varepsilon_f}{F/N} \frac{F/N}{D_f^2 \sigma} = 1 + \text{const} \cdot \frac{F_{R_i} D_f}{\mathcal{E}_f \varepsilon_f} \frac{\mathcal{E}_f \varepsilon_f}{F/N} \,. \tag{4.4}$$

where λ_σ and $(F/N)/(D_f^2\sigma)$ are constants for a fixed force F. Hence, σ_c/σ can be expressed in terms of the parameters $(\mathcal{E}_f\varepsilon_f)/(F/N)$ and $(F_{R_i}D_f)/(\mathcal{E}_f\varepsilon_f)$, respectively reported in Figures 18 and 19. The product $\frac{F_{R_i}D_f}{\mathcal{E}_f\varepsilon_f}\frac{\mathcal{E}_f\varepsilon_f}{F/N}$, which governs the *strength*, is reported in Figure 20 as a function of γ for various values of $\nu_f \in (0, 0.3)$, with variable bending and torsional stiffness at the fiber level ($\mathcal{B}_f/(\mathcal{E}_f\, D_f^2) \in (0, 0.1)$, $\mathcal{T}_f/(\mathcal{E}_f\, D_f^2) \in (0, 0.1)$), which however have a negligible influence. In the same Figure, for comparison, we juxtapose the graph of $\mathcal{E}/N\mathcal{E}_f$, already shown in Figure 15, which represents the *stiffness* of the cable. The case shown corresponds to a ML cable with $M = 100$ layers and considers the state of stress for fibers at $R_i = 30\, D_f$.

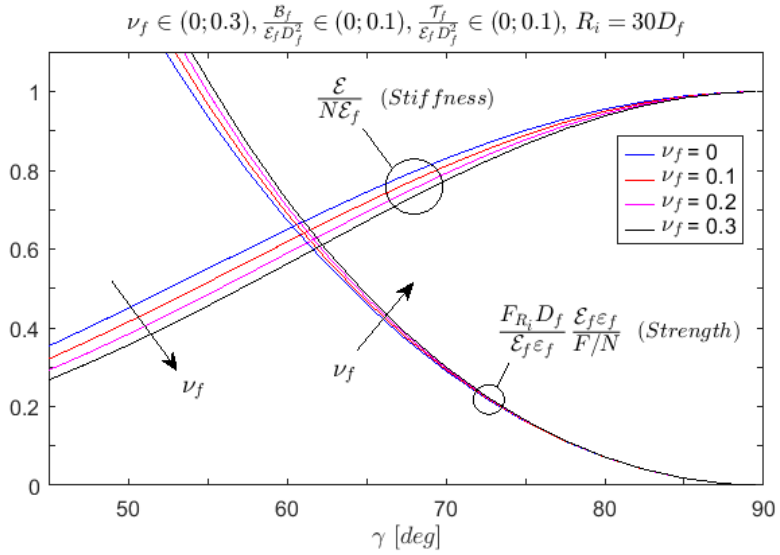

Figure 20: Comparison between the dimensionless parameters $(\mathcal{E}_f \varepsilon_f)/(F/N) \cdot (F_{R_i} D_f)/(\mathcal{E}_f \varepsilon_f)$ and $\mathcal{E}/N\mathcal{E}_f$, respectively associated with the *strength* of a fiber at $R_i = 30\, D_f$ and the overall *stiffness* of a ML cable made of $M = 100$ layers. Parameters are plot as a function of the reference slope angle γ for various values of $\nu_f \in (0, 0.3)$, with variable bending and torsional stiffness at the fiber level $(\mathcal{B}_f/(\mathcal{E}_f\, D_f^2) \in (0, 0.1)$, $\mathcal{T}_f/(\mathcal{E}_f\, D_f^2) \in (0, 0.1))$.

It is apparent that the cable axial stiffness increases with γ, as opposed to the tensile strength. Therefore, a value of $\gamma = 90°$ (straight fibers), which certainly optimizes the cable axial stiffness, may not in general correspond to the maximum strength for the cable, as increasing γ means reducing not only the stress in the cable fibers but also the radial contact forces. These forces are beneficial in terms of strength: on the one hand, the capacity of a broken fiber can be re-established via frictional contact at a certain distance from the point of breakage; on the other hand, transverse compressions can improve the lateral bond between the CNTs (compare Figure 1) and, hence, the strength of the CNTF.

Any quantitative estimate of the effects of the radial contact forces requires consideration of a number of aspects. The fiber strength is not a deterministic property,

but shall be interpreted via a statics, usually of the Weibull type. The strength of the fiber depends on the transverse compression in a way which should also be interpreted statistically. The probability of failure results from the probability that all fibers will break. When the weakest fiber fails, the surviving fibers become more stressed because they have to bear the contribution of the broken filament: in this condition, one has to compute the probability of breaking of a second fiber and so on. Considering the union of all possible failure paths, one obtains the probability of failure of the cable. In this evaluation, it is of paramount importance to calculate the capacity of the broken fiber to re-establish its capacity via frictional contact with the other fibers. The proposed formula (4.4), which should be considered conjectural at this time, only takes into account the effect of transverse compressions on fiber strength; no considerations of interwire deformation [30, 44], friction coefficient and fiber re-arrangement have been proposed in the framework of probabilistic mechanics, but this analysis is certainly beyond the scope of the present study.

5. Conclusions

Carbon NanoTube Fibers (CNTFs) are strong, lightweight, flexible and electrically conductive; since, at least in principle, they can be produced in unlimited length, they appear particularly suitable for being the basic filaments in the manufacture of CNTF cables for advanced structural applications. A theoretical model has been proposed to describe the mechanical properties of stretched and twisted strands or cables made of CNTFs. Compared to geometrically-similar arrangements of steel wires, the limited flexural and torsional stiffness of CNTFs, dictated by the peculiar microstructural organization of the constituent Carbon NanoTubes (CNTs), requires ad hoc modelling.

The approach is variational and considers the minimization of the energy that additively accounts for the contribution of the constituent CNTFs. Using symmetry,

the problem is reduced to the paradigmatic case of an isolated fiber wound onto a cylinder, whose energy is defined in terms of macroscopic descriptors of deformation and the equilibrium states are found to be helixes with constant pitch. It is therefore possible to obtain, as a function of the axial, bending and torsional stiffnesses of the individual CNTFs and their Poisson's ratio, analytical expressions for parameters that govern the tensile and torsional responses (which result to be coupled) of stands made of N fibers (with $N = 2, 3, 4, 7$) and of multilayered cables formed by coaxial circular layers of fibers, as well as information on the internal forces in the constituent fibers. A parametric analysis demonstrates the dominant influence of the fiber axial stiffness and helical pitch; the Poisson's ratio has a limited effect, whereas the contribution of the bending and torsional stiffnesses at the fiber level is negligible in practice. However, torsional stiffness plays a decisive role in manufacturing, inasmuch a pre-twist of a straight fiber is converted into the tortuosity of a helix, coiled to form the strand/cable.

The theoretical model has disclosed important aspects that still need to be corroborated by experiments. If the characterization of the extensional and flexural stiffness of the fibers has been the subject of intense experimental activity corroborated by theoretical studies, little or nothing has been done regarding Poisson's ratio and torsional stiffness, the effect of which should be considered. Another issue of paramount importance concerns the contact forces between the helically wound fibers, which result from the stretching or twisting of the cable. These forces induce a lateral confinement, which can increase the bond between the CNTs that form the CNTFs, thus enhancing their effective strength, as well produce a friction constraint in the event of rupture of one fiber, so as to improve the resilience of the cable. This study has shown that the contact forces increase by reducing the helical pitch of the fibers, although the overall stiffness of the cables shows an opposite trend. Therefore, we expect the existence of an optimal pitch, establishing a compromise between strength

and stiffness.

Although some of the conclusions can be considered at this time only conjectural, because they are not corroborated by testing, the contribution of this article consists in having indicated which aspects still require further study and in having provided the theoretical basis for the design of an experimental campaign, which is the next step in our planned activities.

Competing interests. There are no competing interests to declare.

Funding. This research has been developed under the financial support of Rice University.

Author statement. GM and GRC jointly contributed to the conceptualization of the model and the analytical solution and to the writing of the manuscript. RD supervised the work and revised the manuscript. All authors gave final approval to the final version of the article..

References

[1] K. Lu. The future of metals. *Science*, 328:319–320, 2010.

[2] F. Stüssi. Uber die entwicklung der wissenschaft im bruckenbau, 1964.

[3] F. De Miranda. Long span bridges. Design aspects. *Costruzioni Metalliche*, 4:141–167, 1988.

[4] G. Galilei. *Discorsi e dimostrazioni matematiche intorno a due nuove scienze*. Leida, Olanda, 1638.

[5] G. Galilei. *Two New Sciences, translated by Henry Crew and Alfonso de Salvio*. New York, 1954.

[6] R. DesRoches, G. Migliaccio, and G. Royer-Carfagni. Structures that can be made with carbon nanotube fibers but not with other materials. *J. Eng. Mech.*, 2022 (in press).

[7] S. Iijima. Helical microtubules of graphitic carbon. *Nature*, 354:54–58, 1991.

[8] J.C. Stallard, W. Tan, F.R. Smail, T.S. Gspann, A.M. Boies, and N.A. Fleck. The mechanical and electrical properties of direct-spun carbon nanotube mats. *Extreme Mech. Lett.*, 21:65–75, 2018.

[9] Y. Bai, R. Zhang, X. Ye, Z. Zhu, H. Xie, B. Shen, and et al. Carbon nanotube bundles with tensile strength over 80 GPa. *Nat. Nanotechnol.*, 13:589–595, 2018.

[10] L.W. Taylor, O.S. Dewey, R.J. Headrick, N. Komatsu, N.M. Peraca, G. Wehmeyer, K. Junichiro, and M. Pasquali. Improved properties, increased production, and the path to broad adoption of carbon nanotube fibers. *Carbon*, 171:689–694, 2021.

[11] V. Sabelkin, H.E. Misak, S. Mall, R. Asmatulu, and Kladitis P.E. Tensile loading behavior of carbon nanotube wires. *Carbon*, 50:2530–2538, 2012.

[12] A. Carpinteri and N.M. Pugno. Super-bridges suspended over carbon nanotube cables. *J. Phys. Condens. Matter*, 20:1–8, 2008.

[13] N. Pugno. On the strength of the carbon nanotube-based space elevetor cable from nano to mega mechanics. *J. Phys. Condens. Matter*, 18:1971–1990, 2006.

[14] DEXMAT. Making carbon nanotube yarns, 2022. https://dexmat.com/.

[15] B. Shi, T. Wang, L. Shib, J. Lia, R. Wang, and J. Sun. Highly stretchable and strain sensitive fibers based on braid-like structure and sliver nanowires. *Appl. Mater. Today*, 19:1–9, 2020.

[16] S. Seyedin, S. Moradi, C. Singh, and J.M. Razal. Continuous production of stretchable conductive multifilaments in kilometerscale enables facile knitting of wearable strain sensing textiles. *Appl. Mater. Today*, 11:255–263, 2018.

[17] M.D. McCauley, F. Vitale, S.J. Yan, C.C. Young, B. Greet, M. Orecchioni, S. Perike, A. Elgalad, J.A. Coco, M. John, D.A. Taylor, L.C. Sampaio, L.G. Delogu, M. Razavi, and M. Pasquali. In vivo restoration of myocardial conduction with carbon nanotube fibers. *Circ. Arrhythm. Electrophysiol*, 12(8), 2019.

[18] N. Behabtu, C.C. Young, D.E. Tsentalovich, O. Kleinerman, X. Wang, A.W.K Ma, E.A. Bengio, R.F. Waarbeek, J.J. de Jong, R.E. Hoogerwerf, S.B. Fairchild, J.B. Ferguson, B. Maruyama, J. Kono, Y. Talmon, Y. Cohen, M.J. Otto, and M. Pasquali. Strong, light, multifunctional fibers of carbon nanotubes with ultrahigh conductivity. *Science*, 339:182–185, 2013.

[19] D. Appell. Stairway to the heavens. *Phys. World*, 24:30–34, 2011.

[20] Vigolo B., Penicaud A., Coulon C., Sauder C., Pailler R., Journet C., Bernier P., and Poulin P. Macroscopic fibers and ribbons of oriented carbon nanotubes. *Science*, 290(5495):1331 – 1334, 2000.

[21] M. Adnan, R.A. Pinnick, Z. Tang, W.L. Taylor, S.S. Pamulapati, G. Carfagni-Royer, and M. Pasquali. Bending behavior of cnt fibers and their scaling laws. *Soft Matter*, 14(8284), 2018.

[22] L. Galuppi, M. Pasquali, and G. Royer-Carfagni. The effective tensile and bending stiffness of nanotube fibers. *Int. J. Mech. Sci.*, 163(105089), 2019.

[23] P. Croce. Non-linear behavior of heavy stays. *International Journal of Solids and Structures*, 50:1093–1107, 2013.

[24] G.A. Costello and J.W. Philips. Contact stresses in thin twisted rods. *J. Appl. Mech.*, 40:629–630, 1973.

[25] F. Foti and L. Martinelli. Mechanical modeling of metallic strands subjected to tension, torsion and bending. *Int. J. Solids Struct.*, 91:1–17, 2016.

[26] W.S. Utting and N. Jones. The response of wire rope strands to axial tensile loads - PART I. EXPERIEMNTAL results and theoretical predictions. *Int. J. Mech. Sci.*, 29:605–619, 1987.

[27] S.A. Velinsky. General nonlinear theory for complex wire rope. *Int. J. Mech. Sci.*, 27:497–507, 1985.

[28] G.A. Costello. *Theory of wire rope.* Mechanical Engineering Series. Springer-Verlag, New York, 2nd edition, 1997.

[29] M. Fraldi, G. Perrella, M. Ciervo, F. Bosia, and N.M. Pugno. A hybrid deterministic-probabilistic approach to model the mechanical response of helically arranged hierarchical strands. *J. Mech. Phys. Solids*, 106:338–352, 2017.

[30] I. Argatov. Response of a wire rope strand to axial and torsional loads: Asymptotic modeling of the effect of interwire contact deformations. *Int. J. Solids Struct.*, 48:1413–1423, 2011.

[31] S. Machida and A.J. Durelli. Response of a strand to axial and torsional displacements. *J. Mech. Eng. Sci.*, 15:241–251, 1973.

[32] J.W. Philips and G.A. Costello. Analysis of wire ropes with internal-wire-rope cores. *Applied Mechanics*, 52:510–516, 1985.

[33] H. Ramsey. A theory of thin rods with application to helical constituent wires in cables. *Int. J. Mech. Sci.*, 30:559–570, 1988.

[34] Z.L. Zhao, H.P. Zhao, J.S. Wang, Z. Zhang, and X.Q. Feng. Mechanical properties of carbon nanotube ropes with hierarchical helical structures. *J. Mech. Phys. Solids*, 71:64–83, 2014.

[35] A.E.H. Love. *A treatise on the mathematical theory of elasticity.* Dover, New York, 4th edition, 1944.

[36] W.S. Utting and N. Jones. A survey of literature on the behaviour of wire ropes. *Wire Industry*, 91:623–629, 1984.

[37] C. Jolicoeur and A. Cardou. A numerical comparison of current mathematical models of twisted wire cables under axysimmetric loads. *J. Energy Resour. Technol.*, 113:241–249, 1991.

[38] S.R. Ghoreishi, T. Messager, P. Cartrauud, and P. Davies. Validity and limitation of linear analytical models for steel wire strands under axial loading, using a 3d fe model. *Int. J. Mech. Sci.*, 49:1251–1261, 2007.

[39] E.A.W. de Menezes and R.J. Marczak. Comparative analysis of different approaches for computing axial, torsional and bending stiffnesses of cables and wire ropes. *Eng. Struct.*, 241(112487):1–11, 2021.

[40] F.H. Hruska. Tangential forces in wire ropes. *Wire and wire products*, 28:455–460, 1953.

[41] S. Sathikh, M.B.K. Moorthy, and M. Krishnan. A symmetric linear elastic model for helical wire strands under axysimmetric loads. *Wire and wire products*, 31:389–399, 1996.

[42] M. Labrosse, A. Nawrocki, and T. Conway. Frictional dissipation in axially loaded simple straight strands. *J. Eng. Mech.*, 126:641–646, 2000.

[43] K. Kumar and J.E.Jr. Cochran. Closed-form analysis for elastic deformations of muultilayered strands. *Transactions of the ASME*, 54:898–903, 1987.

[44] F. Foti and L. Martinelli. Modeling the axial-torsional response of metallic strands accounting for the deformability of the internal contact surfaces: derivation of the symmetric stiffness matrix. *Int. J. Solid Struct.*, 171:30–46, 2019.

[45] I. Ostanin, R. Ballarini, and T. Dumitrica. Distinct element method modeling of carbon nanotube bundles with intertube sliding and dissipation. *J. Appl. Mech.*, 81:061004–1, 2014.

[46] R.B. Pipes, P. Hubert, J.P. Salvetat, and L. Zalamea. Flexural deflection as a measure of van der waals interaction forces in the cnt array. *Compos. Sci. Technol.*, 66:1125–1131, 2006.

[47] C. Li and T.W. Chou. A structural mechanics approach for the analysis of carbon nanotubes. *Int. J. Solids Struct.*, 40:2487–2499, 2003.

[48] R.B. Pipes and L. Zalamea. Energetics of imperfectly bonded carbon nanotube arrays in flexure. *Compos. Sci. Technol.*, 66:2844–2854, 2006.

[49] S.S. Antman. *Nonlinear Problems of Elasticity*. Applied Mathematical Sciences. Springer, Pisa, 2nd edition, 2005.

[50] S. Lenci, F. Clementi, and G. Rega. Comparing nonlinear free vibrations of timoshenko beams with mechanical or geometric curvature definition. *Procedia IUTAM*, 20:34–41, 2017.

[51] E. Babilio and S. Lenci. On the notion of curvature and its mechanical meaning in a geometrically exact plane beam theory. *Int. J. Mech. Sci.*, 128-129:277–293, 2017.

[52] E. O. Doebelin and N. Dhanesh. *Measurement systems: application and design*. McGraw Hill, New Delhi, 2007.

[53] G. Migliaccio and G. Ruta. The influence of an initial twisting on tapered beams undergoing large displacements. *Meccanica*, 56:1831–1845, 2021.

[54] G. Migliaccio. Analytical evaluation of stresses and strains in inhomogeneous non-prismatic beams undergoing large deflections. *Acta Mechanica*, 233(7):2815–2827, 2022.

[55] G. Mengali and A. Quarta. *Fondamenti di meccanica del volo spaziale*. Pisa University Press, Pisa, 2006.

[56] G. Ruta, M. Pignataro, and N. Rizzi. A direct one-dimensional beam model for the flexural-torsional buckling of thin-walled beams. *J. Mech. Mater. Struct.*, 1:1479–1496, 2006.

[57] F.P. Pai. Three kinematic representations for modeling of highly flexible beams and their applications. *Int. J. Solids Struct.*, 48:2764–2777, 2011.

[58] R. Courant and D. Hilbert. *Methods of mathematical physics*. Interscience Publisher, New York, 1st edition, 1953.